

Pseudo-Spectral Collocation Methods for Hyperbolic Equations with Arbitrary Precision: Applications to Relativistic Gravitation

Daniel Santos-Oliván · Carlos F. Sopena

the date of receipt and acceptance should be inserted later

Abstract General Relativity is the best theory of gravity that we have so far. It not only provides a relativistic description of the gravitational interaction but also of the spacetime geometry, which makes it quite special in comparison with other theories. The field equations are non-linear partial differential equations that can be arranged as a hyperbolic system of evolution equations together with some constraint equations. The structure of the hyperbolic evolution operator is special in the sense that evolution of smooth initial data leads to smooth solutions, assuming an adequate gauge choice and the absence of matter fields whose evolution can generate shock-type discontinuities. Numerical Relativity consists in the study of formulations of the full Einstein equations together with the development of the corresponding numerical methods/algorithms for the study of problems where a general relativistic description is required, in particular for those with high-accuracy requirements. In this paper, we advocate the use of Pseudo-Spectral Collocation (PSC) methods in combination with high-order bit precision algorithms for this kind of problems. The main reason is that the PSC method provides exponential convergence (for smooth problems, as is the case in many problems in relativistic gravitation) and is very amenable for high-precision arithmetic since we can use different bit precision without the need of changing the structure of the numerical algorithms. Moreover, the PSC method provides high-compression storage of the information. We illustrate these ideas in some problems in relativistic gravitational collapse, whose dynamics exhibits self-similarity properties that require very precise numerical simulations to be properly captured and characterized.

Keywords Hyperbolic problems · Pseudospectral Methods · Arbitrary-precision arithmetic · Numerical Relativity · Gravitational Collapse.

Institut de Ciències de l'Espai (ICE, CSIC), Campus UAB, Carrer de Can Magrans s/n, 08193 Cerdanyola del Vallès, Spain ·
Institut d'Estudis Espacials de Catalunya (IEEC), Edifici Nexus I, Carrer del Gran Capità 2-4, despatx 201, 08034 Barcelona, Spain

1 Introduction

The modelling of physical phenomena requires choosing the appropriate type of numerical algorithm that ensures a satisfactory answer in terms of accuracy and reliability but also in terms of efficiency and computational cost. For many scientific problems, it seems reasonable to think that 64-bit (double precision) floating point arithmetic, roughly fifteen or sixteen significant digits, is enough to obtain accurate results. In some cases, even 32-bit (single precision) floating point arithmetic, seven or eight significant figures, can be sufficient. However, there are problems that demand a very high degree of precision [1]. For instance, in cases where solutions at late times strongly depend on the initial conditions or in cases where the physical properties are very sensitive to the value of certain parameters, the ability to increase the precision of the numerics may become an essential ingredient to reach satisfactory results (see, e.g. [2]).

Different types of numerical algorithms have been used in numerical relativity (for some accounts of Numerical Relativity can be found in [3, 4, 5, 6, 7, 8, 9]). Finite Differences provide simple and easy ways to design algorithms while Finite Element methods are in general more robust and modular, which is the reason why they are very frequently used in engineering problems. Nevertheless, if the priority is to achieve high accuracy then, spectral and pseudospectral methods are a convenient choice due to their great convergence properties: They converge exponentially for smooth problems. It has also been shown that they provide highly precise solutions in a variety of problems, from fluid dynamics to the computation of gravitational-wave templates (see, e.g. [4, 10, 11, 12]).

The main goal of this paper is to show, in the context of Relativistic Gravitation, that the powerful convergence properties of PseudoSpectral Collocation (PSC) methods make them an ideal option to go beyond the typical 64-bit floating-point arithmetic. For this precision, maximum accuracy is usually reached with a relatively quite low number of collocation (discretization) points. Therefore, going beyond this precision does not constitute a high increase in computational cost. In addition, PSC methods provide a high-compression of the information that characterizes the solution of our problem. Indeed, the number of collocation points (or modes in the spectral picture) needed to reach very high accuracy is much smaller than the number of points in other methods (e.g., Finite Differences) so that the memory demands get reduced drastically. Moreover, the structure of the algorithms, and in consequence of the numerical codes that implement them, is independent of the number of collocation points, which is also another advantage of the PSC method since we do not have to touch the algorithms in order to increase the precision, just to change the number of collocation points. This is contrast with Finite Differences methods, where by increasing the number of discretization points within a wide range we reach machine precision and a new Finite Differences algorithm will have to be implemented in our numerical code.

In order to show in practice all these claims, we have developed a new numerical library, **ANETO** (Arbitrary precision solvEr with pseudo-specTral Methods) [13], that we have used in the numerical simulations reported in this paper. The **ANETO** library provides complete freedom in the numerical precision in the sense that we have the possibility of adjusting the bit precision of our algorithms to fulfil the exact accuracy requirements of a given problem. It also contains a tool to translate numerical codes from the standard double precision to arbitrary

precision. The work presented in this paper originates from the experience of the authors in dealing with physical problems in relativistic gravitation, in particular the description of gravitational collapse in several scenarios where gravity is well described by General Relativity (see [14,15]), and where the accuracy requirements on the numerical solutions are very high. The problems in Numerical Relativity (the techniques to solve the field equations of General Relativity by means of numerical methods) to which we have applied the **ANETO** library are about the gravitational collapse of different spherically-symmetric matter configurations. The conclusions of this paper can be easily extrapolated to different one-dimensional evolution problems, i.e. with one space dimension, in other research areas. Despite this simplification, these problems exhibit properties like self-similarity whose analysis led us to go beyond the standard double precision.

The plan of this paper is as follows: In Sec. 2 we briefly review the basic mathematical foundations of the PSC method. In Sec. 3, we show the performance of PSC methods in terms of accuracy and speed for arbitrary precision computations and compare it to the usual floating point arithmetics and also to other popular discretisation methods. We also discuss how parallel computing needs to be included in a practical implementation in order to use high-precision in realistic/complex simulations. In Sec. 4, we describe two examples of evolution problems in the area of General Relativity that show how we can reach accuracies that are very difficult or almost impossible to obtain using double precision. Finally, we have included two appendices: In Appendix A we include some important elements of the PSC method that have been implemented in the **ANETO** library and that, for the sake of clarity, are not part of the main text. In Appendix B we briefly describe the basic features of the **ANETO** library.

2 The PSC Method for the Solution of Differential Equations

Let us consider a general initial-boundary value problem consisting in a system of Partial Differential Equations (PDEs) defined over a spatial domain $\mathcal{D} \in \mathbb{R}^d$, being d the number of space dimensions, and for a time interval $t \in \mathcal{T} \equiv [t_i, t_f] \subset \mathbb{R}$:

$$\mathcal{L}[\mathbf{u}](t, \mathbf{x}) = 0, \quad \mathcal{I}[\mathbf{u}](t_i, \mathbf{x}) = 0, \quad \mathcal{B}[\mathbf{u}](t, \mathbf{W}(t, \mathbf{x})) = 0, \quad (t \in \mathcal{T}, \mathbf{x} \in \mathcal{D}), \quad (1)$$

where $u(t, \mathbf{x})$ denotes the vector of unknown variables; \mathcal{L} is a given differential operator that determines the set of PDEs under consideration; in addition, \mathcal{I} is another given operator representing the initial conditions of our evolution problem; and finally, \mathcal{B} is the operator that determines the boundary conditions at a set of (timelike) hypersurfaces defined by the equations $\mathbf{W}(t, \mathbf{x}) = \mathbf{0}$. In General Relativity the operator \mathcal{L} can be divided into two independent parts: One producing a set of hyperbolic evolution equations and the other hand producing a set of constraint equations that the initial data (expressed here in terms of the operator \mathcal{I}) has to satisfy and the evolution has to preserve.

In spectral methods (see, e.g. [16,17,18] for general accounts) the solution to this type of problems is approximated by using a series of the form:

$$\mathbf{u}_N(t, x) = \sum_{k=0}^N \mathbf{a}_k(t) \phi_k(x), \quad (2)$$

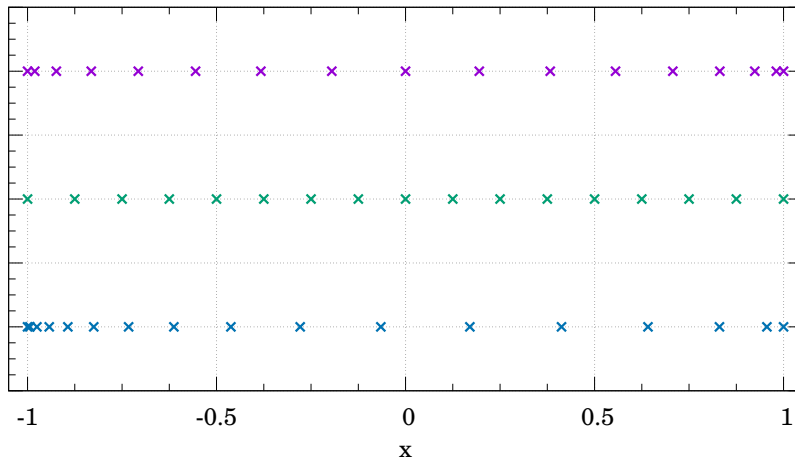


Fig. 1 Different mappings between the Physical and Spectral Grids. The grid at the top (purple) shows the distribution of collocation points in a Lobatto-Chebyshev grid [see Eq. (66)]. The grid in the middle (green) represents a mapping to a uniform (equally spaced) grid. And the grid at the bottom (blue) corresponds to a mapping that produces a high concentration of points near the left boundary. All these mappings are described in Appendix A.3.

where ϕ_k are the basis functions and \mathbf{a}_k are the vectors of (spectral) coefficients associated with the approximation to the vector of unknowns, $\mathbf{u}_N(t, x)$. This approximation would be exact if we allow for an infinite number of terms ($N \rightarrow \infty$), which means that a truncation error is made by taking only a finite number of them. The most convenient choice for the basis functions ϕ_k depends on the particular features of the problem under consideration. For instance, Fourier series are naturally adapted to problems with periodic boundary conditions and spherical harmonics are specially suitable when we are using spherical coordinates. In a general case, and taking into account that in this paper we deal with problems in one space dimension, the a priori best choice are Chebyshev polynomials, defined as follows (more details can be found in Appendix A):

$$T_n(X) = \cos \left[n \cos^{-1}(X) \right] \quad (n = 0, \dots ; X \in [-1, 1]). \quad (3)$$

Notice that here, the coordinate X , which we call the *spectral* coordinate, will not be in general the same as the coordinate x in Eq. (2), which we call the *physical* coordinate. They will have in general different ranges and will be related by a one-to-one mapping¹, $x = x(X) \Leftrightarrow X = X(x)$. Examples of possible mappings, described in Appendix A.3, are shown in Figure 1.

Among all possible spectral methods, in this work we consider the method of collocation, known as the PSC method. It consists in finding the solution by demanding that our equations (1) are exactly satisfied at a set of collocation points. Within the Chebyshev PSC method, the particular choice of collocation points

¹ Although we are not considering it here, it is in principle possible to include a dependence on the time t in this mapping.

that we consider throughout this work is the *Lobatto-Chebyshev* grid of collocation points [see Eq. (66) in Appendix A.1]. This particular choice, apart from minimizing the interpolation error, includes the boundary points, $X = \pm 1$, which allows us to directly impose boundary conditions there.

In the PSC method we have two representations of the approximation to the solution of our problem. The first one, given by Eq. (2) with the choice of basis functions $\phi_k(x) = T_k(X(x))$, is the standard one in spectral methods and hence we call it the *spectral* representation. In this representation, the order of magnitude of the spectral coefficients decays exponentially with the degree, n , of the Chebyshev polynomial:

$$|a_n^k| \sim e^{-\alpha^k n} \quad (k = 1, \dots, \mathcal{N}; n = 0, \dots, N), \quad (4)$$

where α^k is a coefficient associated with the variable u^k . As a consequence, the discretization error due to the use of a finite number of points also decays exponentially. This behaviour is illustrated in Figure 2 for numerical computations using different number of digits of precision. The other type of representation that is used in the PSC method is the *physical* representation, based on the use of the collocation values of our variables, \mathbf{u}_i , and given in Eq. (68). Both representations can be related via matrix transformations or via the Fast Fourier Transformation (FFT) algorithm, which reduces the computational cost of the transformation from $\mathcal{O}(N^2)$ to $\mathcal{O}(N \log N)$.

The possibility of using the FFT algorithm for the change between the physical and spectral representations is of particular relevance for the solution of time-dependent problems described by PDEs. Indeed, we can use the collocation values of our variables, $\mathbf{u}_i(t)$, as the unknowns to be found as the solution of our evolution PDEs. This is particularly useful when we have to deal with non-linear terms, like for instance $u^2 \equiv \mathbf{u} \cdot \mathbf{u}$, since the collocation values of this quantity are simply $u_i^2 = \mathbf{u}_i \cdot \mathbf{u}_i$. In contrast, in the spectral picture, the spectral coefficients of u^2 are given as a double sum over the spectral index. In general, for any function of \mathbf{u} , say $\mathbf{f}(\mathbf{u})$, the collocation values can be immediately found as: $\mathbf{f}(\mathbf{u})_i = \mathbf{f}(\mathbf{u}_i)$. Therefore, nonlinear terms in the PDEs can be dealt in a simple and natural way within the PSC method using the physical representation. At the same time, the change between the physical and spectral representations also allows us to deal in a simple way with more complex operators than algebraic ones. In particular, with differentiation and integration, which are operations that are simpler in the spectral representation than in the physical one. In the physical representation these operations can be performed by using a matrix multiplication that involves all the values of our variables in the collocation grid (meaning $\sim \mathcal{O}(N^2)$ operations), while in the spectral representation only involves linear operations on the spectral coefficients, in addition to the FFTs for the change of representation, and hence it means $\sim \mathcal{O}(N \log N)$ operations again. More details are given in Appendix A.4.

2.1 The Multidomain PSC Method

Up to this point we have assumed that our computational domain can be mapped to a single Lobatto-Chebyshev spectral domain ($[-1, 1]$). However, in some applications, different regions of our computational domain may require different degrees of spatial resolution and hence, the single-domain approach is not very

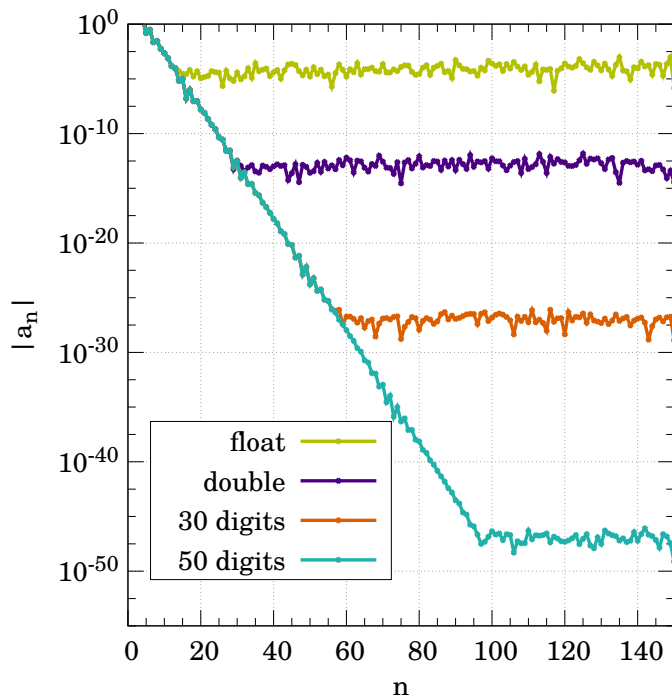


Fig. 2 Representation of the Spectral Coefficients. For a smooth enough function (for this plot we have used the function $f(x) = \exp(\tan(x))$) the modes in the spectral representation decay exponentially until they reach the precision error of our computations. With the use of arbitrary precision (more number of digits) we can control the level of the computer round-off error.

effective and some form of grid refinement needs to be adopted. In the case of the PSC method, a simple choice is to use a multidomain scheme that distributes the subdomains so that regions where high resolution is required are covered by more subdomains than regions less demanding in terms of resolution. For the case of evolution problems in one spatial dimension we consider a decomposition of our physical computation domain $\Omega = [x_L, x_R]$ in D disjoint subdomains:

$$\Omega = \bigcup_{a=0}^{D-1} \Omega_a, \quad \Omega_a = [x_{a,L}, x_{a,R}], \quad (5)$$

with the identification: $x_{a,R} = x_{a+1,L}$ ($a = 0, \dots, D-2$). Each subdomain Ω_a is mapped into the spectral domain $[-1, 1]$. For our computations we assume a simple linear mapping but other mappings, like the ones considered in Fig. (1) and described in Appendix A.3, are possible. Then, given the coordinate x of a point in the physical domain Ω , assuming it belongs to the subdomain Ω_a , it is mapped to a spectral coordinate X_a according to the following linear mapping:

$$x \longrightarrow X_a(x) = \frac{2x - x_{a,L} - x_{a,R}}{x_{a,R} - x_{a,L}}. \quad (6)$$

The inverse mapping is:

$$X_a \longrightarrow x(X_a) = \frac{x_{a,R} - x_{a,L}}{2} X_a + \frac{x_{a,L} + x_{a,R}}{2}. \quad (7)$$

and the Jacobian of the transformation is simply given by:

$$\frac{dx}{dX_a} = \frac{x_{a,R} - x_{a,L}}{2}. \quad (8)$$

As we can see, the Jacobian is different from subdomain to subdomain unless all of them have the same physical coordinate size. Despite its simplicity, the linear mapping can be used for refinement adapting the length of each subdomain to the resolution needs of the problem under consideration. All what we need is a refinement criteria for the adaptation of the subdomain sizes.

In order to use a multidomain scheme, we need to adapt the PSC single-domain operations described above. For most of the operations, the generalization to a multidomain scheme is straightforward since the operation can be performed independently subdomain by subdomain, thus we are not going to discuss them here. However, some operations require some extra ingredients in order to work in the multidomain framework. These extra ingredients are related to the communication between subdomains or to the imposition of boundary conditions. The case of differentiation is a good example. In principle, we can perform derivatives in a multidomain scheme by performing the differentiation at each subdomain separately. However, it is well-known (see also Sec. 3 in this paper) that the computation of derivatives in the PSC method becomes noisy producing an accumulation of error at the points near the boundaries. We can take advantage of the multidomain scheme in order to reduce this kind of error by using a dual grid scheme. The idea is to use a second grid constructed such that the boundaries of the subdomains coincide with the middle points of the subdomains of the main (original) grid (see Figure 3). In this way, the dual grid has $D + 1$ subdomains, $\{\Omega_{\bar{a}}\}_{\bar{a}=0,\dots,D}$, with the left boundary location of each subdomain, say \bar{a} ($= 0, \dots, D$), being given by $\bar{x}_{\bar{a},L} = (x_{\bar{a}-1,L} + x_{\bar{a}-1,R})/2$ (excepting for $\bar{a} = 0$, in which case it is simply the global left boundary point x_L), and the right boundary location is given by $\bar{x}_{\bar{a},R} = (x_{\bar{a},L} + x_{\bar{a},R})/2$ (excepting for $\bar{a} = D$, in which case it is simply the global right boundary point x_R). When we compute the derivative in the dual grid, the points where typically the error is the lowest coincide with the location where the error is typically the greatest in the subdomains of the main grid. Then, we compute the final derivative of our function by combining the derivatives computed separately in the main (f'_{main}) and dual (f'_{dual}) grids. For a given point x belonging to the subdomain Ω_a of the main grid, the derivative is the following weighted sum of the derivatives from the main and the dual grids:

$$f'(x) = \pi_a(x) f'_{\text{main}}(x) + (1 - \pi_a(x)) f'_{\text{dual}}(x) \quad (x \in \Omega_a), \quad (9)$$

where $\pi_a(x)$ is a weighting function on the subdomain Ω_a of the main grid (this function together with $1 - \pi_a(x)$ form a partition of unit associated with the subdomain Ω_a) that takes values between zero and one, being zero in the boundaries of the subdomains of the main grid and one at the boundaries of the dual grid.

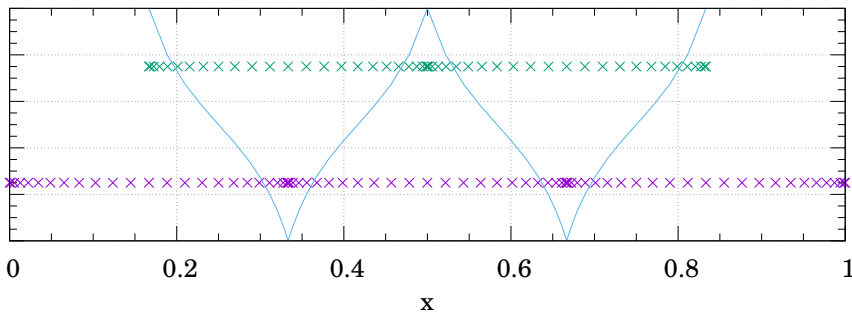


Fig. 3 Structure of a Dual Grid. Schematic representation that shows the structure of a particular implementation of a dual grid scheme. The main grid (in purple) is composed of three subdomains and the dual grid (in green) is shifted and has four subdomains (one more), but we do not show the subdomains that contain the global boundaries, which require a special treatment, just the two interior subdomains. The blue line shows the weighting function $\pi_a(x)$ of Eq. (10).

Moreover, it is smooth between the boundary and the centre of the subdomain. One example of a partition function is:

$$\pi_a(x) = \begin{cases} \frac{(x-x_{a,L})(x-x_{a,R})}{(x-x_{a,L})(x-x_{a,R})+(x-\bar{x}_{a,L})(x-\bar{x}_{a,R})} & \text{if } x \in \bar{\Omega}_a, \\ \frac{(x-x_{a,L})(x-x_{a,R})}{(x-x_{a,L})(x-x_{a,R})+(x-\bar{x}_{a+1,L})(x-\bar{x}_{a+1,R})} & \text{if } x \in \bar{\Omega}_{a+1}. \end{cases} \quad (10)$$

This structure of $\pi_a(x)$ is due to the fact that a given point of the subdomain Ω_a can either be at the subdomain $\bar{\Omega}_a$ or $\bar{\Omega}_{a+1}$ of the dual grid (see Figure 3).

On the other hand, when solving PDEs using a multidomain scheme it is necessary to specify how to communicate the different subdomains, and this depends on the spacetime (characteristic) structure of the PDE system. Here, we are going to discuss how to use the multidomain PSC method to solve hyperbolic PDEs (we assume that our equations are strongly hyperbolic in the sense described in [19, 20] and also briefly below). At the boundaries between subdomains we have two points, the right boundary of the subdomain to the left ($x_{a,R}$) and the left boundary of the subdomain to the right ($x_{a+1,L}$), which are identified since they represent the same physical point. Although in principle we should solve the PDEs at both points, the hyperbolic structure of the PDEs imposes constraints on how to assign values to the PDE variables at these “two” points. To understand how to do this in practice, let us consider a general hyperbolic PDE system in $1 + 1$ dimensions (time t and spatial coordinate x) in first-order form:

$$\partial_t \mathbf{W} + \mathcal{A}[x, \mathbf{W}] \cdot \partial_x \mathbf{W} = \mathbf{S}[x, \mathbf{W}], \quad (11)$$

where here \mathbf{W} is the vector of independent variables, \mathcal{A} is the matrix that determines the characteristic structure (see, e.g. [19] for details) of the PDEs, and \mathbf{S} is a source vector that depends on the coordinate x and the variables \mathbf{W} . The hyperbolic character of the PDE problem is determined by the following eigenvalue problem:

$$\mathcal{A} \cdot \mathbf{E} = \lambda \mathbf{E}, \quad (12)$$

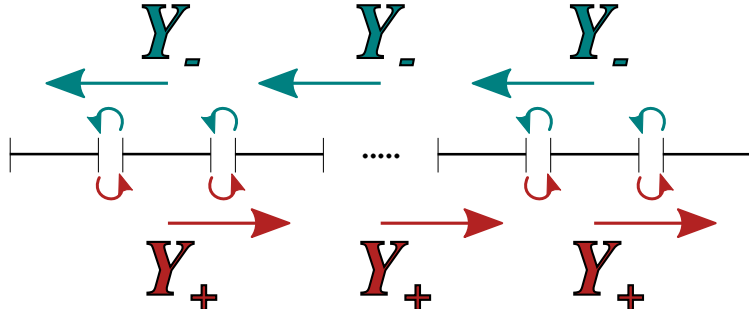


Fig. 4 Diagram of the Multidomain Structure for PSC Methods. The evolution variables need to be communicated between subdomains using the characteristic variables, Y_- and Y_+ , which have a well-defined speed and direction of propagation. The communication is done by copying the boundary values in the direction indicated by the arrows.

where \mathbf{E} is a vector in the space of the PDE variables \mathbf{W} . If there is a complete set of eigenvectors and all the eigenvalues are real the system is said to be *strongly hyperbolic*. The eigenvectors of the matrix \mathcal{A} correspond to the different characteristic fields of the system and the eigenvalues to the characteristic speeds associated with the characteristic fields. We can then choose a new set of PDE variables consisting of the characteristic fields (say \mathbf{Y}), which have a well-defined propagation speed, the eigenvalues λ , and rewrite Eq. (11) as:

$$\partial_t \mathbf{Y} + \mathcal{D}_A \partial_x \mathbf{Y} = \tilde{\mathbf{S}}(x, \mathbf{Y}), \quad (13)$$

where \mathcal{D}_A is the diagonal matrix containing the eigenvalues λ . Given that these eigenvalues are real and represent the propagation speed of the characteristic \mathbf{Y} , some of the variables in \mathbf{Y} will have positive speed, say \mathbf{Y}_+ , and others will have negative velocity, say \mathbf{Y}_- . This knowledge is crucial to update the points at the boundaries between subdomains as follows (see Figure 4): Given two subdomains, Ω_a and Ω_{a+1} , with common boundary points $x_{a,R}$ (right boundary of Ω_a) and $x_{a+1,L}$ (left boundary of Ω_{a+1}), the fields with positive speed, \mathbf{Y}_+ , are evolved at $x_{a,R}$ using the PDEs in Eq. (13) and the values obtained are copied to the corresponding variables at the point $x_{a+1,L}$. Conversely, the fields with negative speeds are evolved at $x_{a+1,L}$ using the PDEs and the resulting values are copied to the corresponding variables at the point $x_{a,R}$. Finally, the characteristic variables are not only important to deal with the boundaries between subdomains, they can also be used to impose boundary conditions at the global boundaries in a clear and simple manner, for instance for the case of in/outgoing boundary conditions.

3 Synergies between the PSC method and arbitrary precision

The representation of real numbers with a large number of significant digits in the limited memory of a computer is a delicate issue. The usual solution is the so-called *floating-point* representation, similar to scientific notation, where a given

real number x can be expressed as:

$$x = \left(1 + \sum_{i=1}^{b_m-1} b_i \times 2^{-i} \right) \times 2^E, \quad (14)$$

where b_m is the number of bits of the mantissa and E of the exponent. The number of bits dedicated to E is important because it establishes the maximum range of our variables. However, we are more interested in the influence of b_m since it sets the machine precision, also known as round-off error, as follows:

$$\text{error} = \lceil \text{bits} \cdot \log_{10}(2) \rceil. \quad (15)$$

The standard numerical precisions that we consider for reference are: *single precision*, where $b_m = 24$ (eight significant digits); *double precision*, with $b_m = 53$, corresponding to 15 – 16 significant digits; and *quadruple precision*, where $b_m = 113$, corresponding to approximately 34 significant digits.

In what follows we discuss the advantages of using the PSC method in combination with arbitrary numerical precision for solving hyperbolic problems with the structure indicated in Eq. (1). We argue that the PSC method allows different bit precisions without the need of changing the algorithm code implementation and at the same time the storage of information required is lower than in other methods. We also discuss the performance of the PSC method for different bit precisions and compare the results with those from other discretization methods. All the PSC algorithms we use in this work have been developed using the **ANETO** library. Details about the structure of this library can be found in Appendix B.

3.1 Numerical Integrals

We start by studying the precision in the computation of an integral using the quadrature methods mentioned previously and described in Appendix A.4. As a test function we use a simple cosine function:

$$f(x) = \cos(x), \quad (16)$$

We consider the computation of the integral of this function over the spectral domain $[-1, 1]$ for different bit precisions and both for single and multidomain setups. The results are shown in Figure 5. The plot on the left shows that as long as one uses enough collocation points the error scales with the round-off error as expected. This is true even for a number of collocation points as low as $N = 47$ up to 260 bits of precision, when the error saturates because the discretization error becomes more important than the round-off error. We have also seen that it is enough to use $N = 71$ collocation points to decrease the error up to 10^{-120} . The same behaviour is shown on the right plot of Figure 5 for the case in which we use a multidomain scheme with only four subdomains ($D = 4$) and $N = 23$ and $N = 47$ collocation points per subdomain. In the first case, $N = 23$, the discretisation error is reached around 10^{-50} but, for the second one, $N = 47$, we can easily reach again 10^{-120} . The horizontal lines in the figure show the round-off error for the single, double, and quadruple precisions respectively, which is obviously much higher than the error we can reach using arbitrary precision.

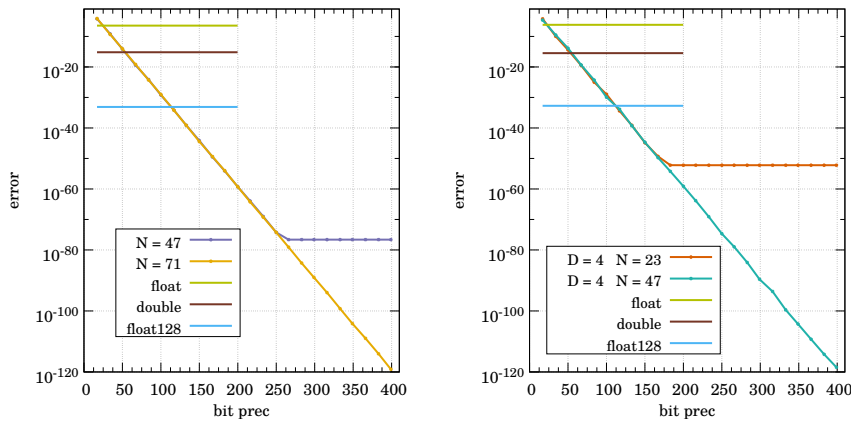


Fig. 5 Maximum Error in the computation of an Integral for Different Bit Precision. The left plot shows the error made by the integration routine in the case of the cosine function integrated on a single Lobatto-Chebyshev collocation grid. The plot on the right shows the same error but when using the multidomain PSC method. In both cases, the points show the errors made for two different number of collocation points with respect to the bit precision used. The horizontal lines indicate the error for single, double, and quadruple precision.

Notice that thanks to the exponential convergence of the PSC method (for smooth solutions) it is easy to obtain very small errors with a relatively low number of collocation points. In the previous example we have reached a very small numerical error (see Figure 5) with less than two hundred collocation points. Although the integral under consideration involved a simple function, we have checked that the same is true independently of the integrand, just restricting ourselves to smooth functions. Figure 5 indicates that in the multidomain scheme the total number of collocation points needs to be higher to obtain a similar error level as in the single domain case, but it has the advantage that, in general, it is faster and more flexible for other operations.

The accuracy that PSC methods are capable to reach is even more clear when we compare it with other discretization methods. In the left plot of Figure 6, we compare the results obtained using the **ANETO** library to Newton-Cotes (NC) formulae [21] of fourth and eleventh orders (a Finite Differences algorithm). In both cases, we set manually the points near the boundaries of the subdomain to avoid the problems associated with the borders. The NC formula of eleventh order seems to be good enough to achieve a reasonable accuracy but the polynomial dependence of the error makes it very difficult to reach accuracies beyond 10^{-50} , while with the PSC method accuracies of the order of 10^{-300} are within reach by using just 100 collocation points. Another relevant comparison is to look at the computational time required for a given accuracy for the two methods. This is shown in the right plot of Figure 6. In the case of the PSC method, we distinguish the case of using the matrix transformation versus the FFT algorithm for the transformation between the physical and the spectral representations. The plot clearly shows that the PSC method achieves high accuracies in much less time that the NC formulae. It also shows that the use of the FFT algorithm for the transformation between representations is also more efficient than the matrix transformation as

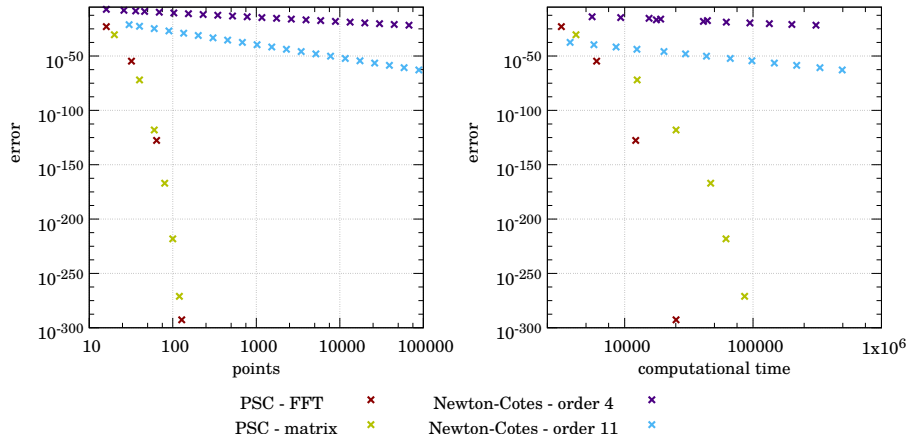


Fig. 6 Comparison between the PSC method and Newton-Cotes formulae for numerical integrals. We compare the error made in the computation of the integral of our test function, Eq. (16), using the PSC method, both with the matrix transformation (yellow points) and the FFT transformation (red), and two different Newton-Cotes formulae, one of fourth order (dark blue) and another one of eleventh order (light blue). In the left plot we compare the error made with the different methods in terms of the number of points used. In the right plot we compare the computational time required by each method to achieve a certain level of accuracy.

expected. Going back to the comparison between the Finite Differences and PSC methods, it is clear that the development of a numerical code to implement the NC formulae is always easier than the development of a PSC numerical code. However, the PSC code does not need to be modified in order to go to very high precisions while improving the Finite Differences code for taking advantage of the potential accuracy usually requires to increase the order of the Finite Differences algorithm. This last option can be very challenging and, for high accuracy, it will not beat the exponential convergence of the PSC method.

3.2 Solving Ordinary Differential Equations with the PSC method

To illustrate the use of the PSC method let us consider the following second-order linear Ordinary Differential Equation (ODE):

$$\frac{d^2 f(x)}{dx^2} + \frac{df(x)}{dx} = e^x, \quad x \in [-1, 1], \quad (17)$$

with boundary conditions,

$$f(-1) = \frac{e}{2}, \quad \frac{df}{dx}(-1) = \frac{e}{2}. \quad (18)$$

This problem has a unique analytical solution given by:

$$f(x) = \frac{1}{2}e^x. \quad (19)$$

The ODE in Eq. (17) can be discretised using the PSC method by imposing it on each collocation point $\{X_i = x_i\}$ of a Lobatto-Chebyshev grid [see Eq. (66)]:

$$\sum_{j=0}^N \left(\mathcal{D}_{xx}^{ij} + \mathcal{D}_x^{ij} \right) f^j = e^{x_i}, \quad (20)$$

where \mathcal{D}_x^{ij} and \mathcal{D}_{xx}^{ij} are the first- and second-order differentiation matrices respectively (see Appendix A and [17, 18, 22]), and f^i are the values of the “unknown” function $f(x)$ at the collocation points. The explicit expression for the differentiation matrices can be found in Eqs. (92) and (93) of Appendix A.4.

We solve this problem by using the PSC method and a sixth-order Finite Differences scheme with uniformly distributed grid points. For the case of the Finite Differences scheme, the first-order differentiation matrix, at the interior points of the domain, can be written as follows:

$$\sum_{j=0}^N \mathcal{D}^{ij} f^j = \frac{-f^{j-3} + 9 f^{j-2} - 54 f^{j-1} + 54 f^{j+1} - 9 f^{j+2} + f^{j+3}}{60 \Delta x}. \quad (21)$$

The comparison between the two methods is shown in Figure 7 where we plot the error, relative to the analytic solution in Eq. (19), as a function of the number of grid points used in each method. In the previous section we already saw that the exponential convergence of the PSC method provides very good accuracy with a relatively small number of collocation points. This property of the PSC method is crucial in this case because the solution involves inverting a matrix [see the discretized version of the ODE with the PSC method in Eq. (20)] whose number of elements is N^2 . In this sense, it is important to realize that the differentiation matrices in the case of the PSC method are sparse [see Eqs. (92) and (93) of Appendix A.4] while in the Finite Differences method its sparsity depends on the stencil (number of points needed for evaluating the derivative). Therefore, in general, the cost of inverting the matrix will be much bigger in the case of the PSC method for a similar number of grid points. Nevertheless, this advantage turns out not be important when we look for high accuracy, in which case the spectral convergence of the PSC method outperforms the Finite Differences method.

3.3 Double versus Arbitrary Precision: Computational Time

We have seen that the combination of the PSC method with arbitrary precision arithmetics is a powerful computational tool that exploits the synergies between the two techniques. The next step is to study in more detail the computation cost of using it. Most of the available computers nowadays use a 64-bit processor that is highly optimised to work with double precision. Going beyond this precision usually requires a software implementation that slows down the computation. The question is how much slow down can be expected depending on the precision that we need to use.

To answer this question we use the test case consisting in the integral of Eq. (16). We quantify the cost for four different grid configurations characterized by the pair (D, N) : D is number of subdomains, and N is the number of collocation points per subdomain]. These four grid configurations are: (i) $(D, N) = (14, 64)$;

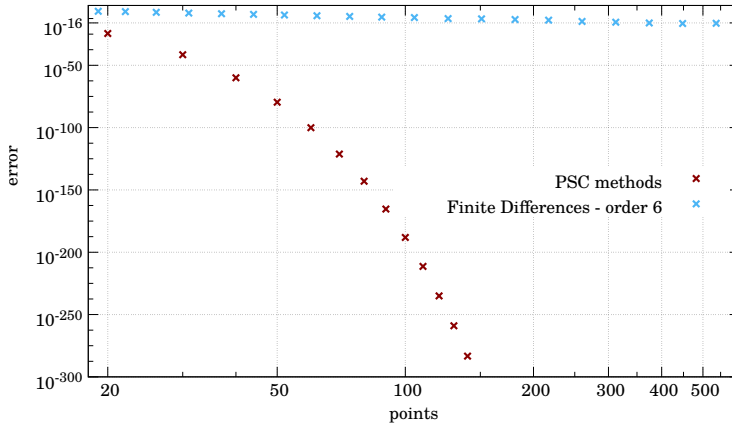


Fig. 7 Comparison of the performance of the PSC and Finite Differences methods for ODE solving. This plot shows the error in solving the second-order ODE in Eq. (17), with boundary conditions in Eq. (18), with respect to its exact solution given in Eq. (19), for both the PSC and Finite Differences numerical methods, with respect to the number of grid/collocation points used in the numerical computation.

(ii) $(D, N) = (14, 128)$; (iii) $(D, N) = (50, 64)$; and (iv) $(D, N) = (14, 127)$. The results are presented in Figure 8, where we can see how much slower is the use of arbitrary precision as compared with the standard double precision. In the range analysed, until 512 bits, or around 150 significant digits, the computational time seems to increase linearly with the number of bits, being a factor 150-300 times slower than the double precision case. Moreover, we have to take into account that in order to take advantage of the additional significant digits we need to increase the number of subdomains and/or collocation points. Nevertheless, using the PSC method we do not need to change our numerical code, just the pair (D, N) . These considerations are important to estimate whether arbitrary precision can be a good solution for a given numerical problem.

Looking at Figure 8, it is also worth mentioning the jumps in the computational cost every time we cross a vertical line (corresponding to multiples of 64 bits). Although the general behaviour is linear, at small scales the function is more or less flat, increasing in multiples of 64 bits. This is not surprising because the tests have been done using a 64-bit processor and are related to the way the library uses double precision numbers to store the arbitrary floating points variables.

3.4 Shared-memory parallelization of PSC computations using arbitrary precision

We have just seen that one of the drawbacks of using arbitrary precision is the loss of computational speed. Given that most current computer processors are designed for 64-bit precision computations, arbitrary precision libraries usually emulate this using symbolic calculations or by means of a software layer that implements the arbitrary precision operations using 64-bit data. Both options significantly slow down the computations that in our case can be of the order of 150 – 300 times.

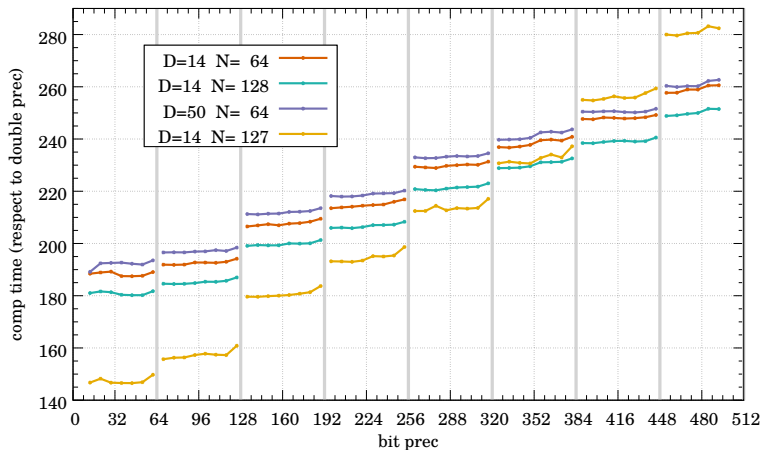


Fig. 8 Computational Time versus Arbitrary Precision. The plot shows the computational time employed in the integration of the test function discussed in Sec. 3.1 for four different grid configurations characterized by the pair (D, N) [D = number of subdomains, and N = number of collocation points per subdomain]. The computational times shown are relative to the computational time corresponding to double precision. The computational time appears to increase linearly with the bit precision. The vertical lines just separate multiples of 64 bits. The computational time experiences a jump at these boundaries, as expected, due to the CPU architecture. The runs with $N = 64$ and $N = 128$ use the FFT algorithm to transform between the physical and spectral representations, while the one with $N = 127$ uses the matrix transformation. As a consequence, the computations for the grid configuration $(D, N) = (14, 127)$ are much slower, in absolute computational time, than the ones for $(D, N) = (14, 128)$.

In order to alleviate this downside of the method we can resort to parallelization. Indeed, the use of parallel computing adapts perfectly to our pseudospectral multidomain scheme because most of our computations are done independently within each of the subdomains. For instance, in the case of derivatives, they can be trivially parallelized because they are defined at each subdomain independently. Instead, in the case of global integrals (integrals over the whole computational domain) it is a bit more complex but they can be adapted without affecting the scaling with the number of operations. To see how we can parallelize integrals, let us consider the example of an indefinite integral of a given function $g(x)$ considered over the whole computational domain Ω and with a boundary condition at the left global boundary x_L (see Appendix A.4):

$$I_L(x) = I_L^b + \int_{x_L}^x dx' g(x'). \quad (22)$$

where $I_L^b = I_L(x_L)$ is the boundary condition that avoids the presence of an arbitrary constant as in usual indefinite integration. Since x is an arbitrary point it can belong to any subdomain Ω_a and then this integral may appear as a serial computation that is difficult to cast into a parallel one because the result depends on the integral for smaller values than x_L . Nevertheless, we can parallelize the computation in the following way: First of all, let a be the number of the subdomain to which x belongs ($x \in \Omega_a$). Then, we can divide the integral into the sum

of partial integrals that can be computed individually at each subdomain:

$$I_{L,d}^p = \int_{x_{d,L}}^{x_{d,R}} dx g(x) = \int_{-1}^1 dX \left(\frac{dx}{dX} \right)_X g(x(X)) \quad (d = 0, \dots, a-1), \quad (23)$$

and the integral of the subdomain of x (Ω_a):

$$I_{L,a}(x) = \int_{x_{a,L}}^x dx' g(x') = \int_{-1}^{X(x)} dX' \left(\frac{dx}{dX} \right)_{X'} g(x(X')), \quad (24)$$

so that the full integral can be computed as:

$$I_L(x) = I_L^b + \sum_{d=0}^{a-1} I_{L,d}^p + I_{L,a}(x) \quad (x \in \Omega_a). \quad (25)$$

With this separation, each piece in the sum can be computed independently in parallel in each subdomain. To implement this in practice, we propose the use of shared-memory parallelization, and more specifically, the broadly used application programming interface OpenMP [23]. This appears to be the simplest option to profit from the possibility of having independent computations in the different subdomains and adding the minimum possible communication overhead. In order to test this we have carried out a number of numerical experiments using OpenMP. The measure of the computational time speedup that we use, S_p , is a function of the number of cores employed, p , defined as:

$$S_p = \frac{T}{T_p}, \quad (26)$$

where T is the computational time spent by a sequential computation and T_p is the time corresponding to a computation that uses p cores. Of course, the ideal unreachable limit is $S_p = p$. Within this framework we have performed tests for integration and differentiation with the parallel multidomain PSC method. This has been done both for double and quadruple (`float128`) precisions. The results for the computational speedup S_p are shown in Figure 9. We can see that we are very close to the maximum speed-up which is indicated by a dashed line in the plot. It is also interesting to note that the differentiation computations are closer to full parallelism than the integration ones. This is expected from the fact that differentiation can be carried out fully independently at each subdomain while for integration we need to communicate the value of the partial integrals.

Up to here we have discussed how to parallelize the operations using the multidomain framework so that each core is in charge of the operations of one or more subdomains, but in any case, it is clear that the subdomain is the minimum unit of parallelization. However, this approach does not address the principal motive for the slowdown, the emulation of the fundamental operations. This is a question currently under investigation in projects like [24], where arbitrary precision numbers are represented as an expansion of double precision numbers of different magnitudes and then the idea is to take advantage of parallel computations with graphics processing units (GPUs) to implement these basic operations.

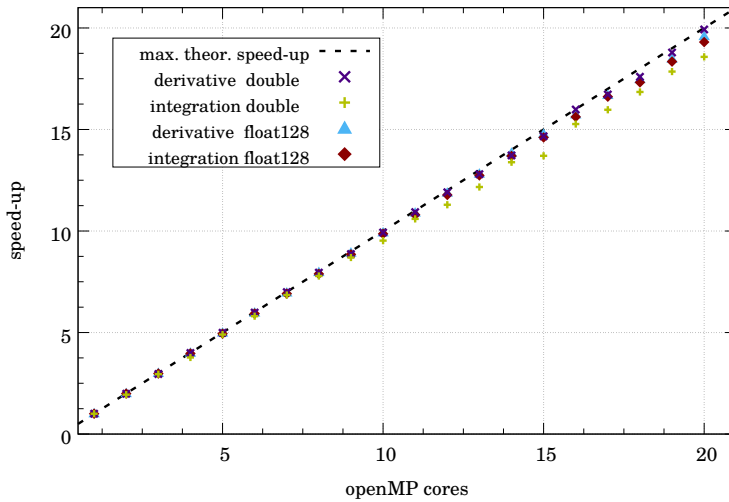


Fig. 9 Speed-up with OpenMP for multidomain PSC computations. This plot shows the computational speed-up, as defined in Eq. (26), for integration and differentiation algorithms with both double and quadruple precision. Differentiation presents a better speed-up but both cases show that the multidomain method is a very good option for parallelization.

3.5 Multidomain Derivatives: The Dual Grid

The computation of derivatives at points near the boundaries between subdomains tends to accumulate a significant error, which in some cases can be one or two orders of magnitude higher than in other more central regions of the subdomain. This phenomenon, known as Runge’s phenomenon [25,26], gets worse as we increase the number of collocation points. As we already mentioned in Secs. 2.1 and B.2, we can deal with this problem by using a dual-grid structure as the one shown in Figure 3. We have carried out several numerical experiments to assess the use of the dual-grid structure by comparing with computations on a single grid. The results are summarized in Figure 10. In the top-left plot we show the error in the computation of a derivative using ten subdomains. It is easy to find in the plot the location of the boundaries between the subdomains since the error exhibits there a peak that in most cases is one order of magnitude higher than the average. The brown line of the bottom-left plot shows the error when we perform the same computation but using the dual-grid scheme. As we can see, the peaks have completely disappeared and the error in the derivative looks now quite flat. This improvement can be seen on the top-right plot of Figure 10, where we present the ratio between the differentiation errors with and without using the dual grid. Near the boundaries our computation has improved between one and two orders of magnitude in terms of the error. We have done the same comparison for the second-order derivative, which is shown in the bottom-right plot. As we can see, the improvement is even better than in the case of the first-order derivative, and the error at all the boundaries has been reduced in two/three orders of magnitude.

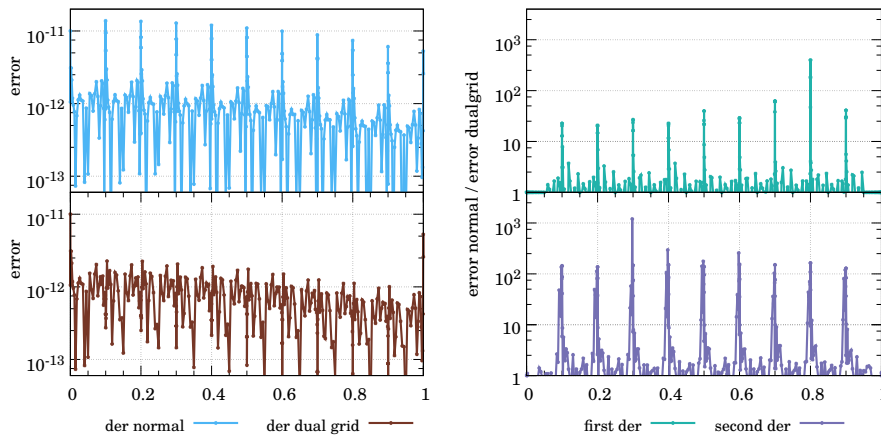


Fig. 10 Dual-Grid Differentiation. The plots on the left show the error in the first-order derivative computed with the dual-grid setup (bottom) and without it (top). We see that at the boundaries across subdomains there is an efficient reduction of the error by eliminating the peaks. The magnitude of the improvement can be seen in the top right plot. The quotient of the error in both cases tells us that the improvement at the points near the boundaries is between one and two orders of magnitude. The bottom right plot shows the same for the second-order derivative where the improvement increases by two or three orders of magnitude.

4 Applications to Numerical Relativity: Gravitational Collapse in different Physical Scenarios

The main motivation for this work, and the reason why we have developed the numerical tools described here, is the study of gravitational collapse in the context of the General Theory of Relativity, known simply as General Relativity (see e.g. [27, 28, 29, 30] for general accounts). The main idea behind General Relativity is that gravity is no longer a force but the manifestation of the curvature of spacetime due to the presence of distributions of energy and momentum. Then, the mathematical description requires the use of the language of differential geometry (see [28, 31] for presentations of differential geometry applied to General Relativity), where the spacetime is identified with a Lorentzian manifold in 3+1 dimensions (three space-like and one time-like dimensions) and the gravitational field is described by the Lorentzian² metric tensor associated with it, $g_{\mu\nu}$ ($\mu, \nu = 0, 1, 2, 3$; usually $\mu = 0$ is the time index and the others are indices associated with space directions). Then, the dynamics of the gravitational field is the dynamics of the spacetime metric. The field equations tell us how the spacetime gets curved by the presence of matter distributions and, at the same time, the metric determines the dynamics of the matter fields in the spacetime it defines. Because of this, the field equations turn out to be nonlinear. They were proposed by A. Einstein in 1915 [32] and they look as follows (we are choosing physical units in which $c = 1$ and $4\pi G = 1$):

$$R_{\mu\nu} - \frac{1}{2}g_{\mu\nu}R + \Lambda g_{\mu\nu} = 2T_{\mu\nu}. \quad (27)$$

² The signature of a Lorentzian metric associated with a (3+1)-dimensional spacetime is $(-1, 1, 1, 1)$. That is, the metric it is not a positive definite matrix.

On the left-hand side of these equations we find the spacetime geometry quantities: $R_{\mu\nu}$, the Ricci Tensor associated with the metric tensor $g_{\mu\nu}$ (both are symmetric tensors); R is the scalar of curvature, which can be obtained as the trace of the Ricci tensor using the inverse metric tensor: $R = g^{\mu\nu} R_{\mu\nu}$. Both the Ricci tensor and the scalar curvature are obtained exclusively from the metric tensor and its derivatives up to second order. They contain non-linear terms in the metric itself and in its first-order derivatives. The last term on the left-hand side is also proportional to the metric, but the proportionality constant is the well-known cosmological constant, Λ , which is mainly used in cosmological scenarios. On the right-hand side of Einstein's equations we find the sector corresponding to the matter fields, the energy-momentum tensor $T_{\mu\nu}$, another symmetric tensor that tells about the distribution of mass, energy, and momentum in the spacetime. These equations are invariant under general changes of spacetime coordinates (diffeomorphism invariance): $x^\mu \rightarrow x^{\mu'} = x^{\mu'}(x^\nu)$. This freedom of coordinates, also known as gauge freedom, means that there are more variables than degrees of freedom. Therefore, four out of the ten Einstein field equations are *constraint* equations (in contrast to evolution hyperbolic equations) that have to be imposed on the components of the gravitational field, the metric. It is enough to impose the constraints on the initial data because it turns out that the rest of the Einstein field equations, the evolution equations, guarantee that once satisfied initially the constraints will also be satisfied along the evolution. Another crucial property of these equations is that the geometric part is divergence-free with respect to the canonical Levi-Civita connection (see [28,31]) and this implies the local conservation of the energy-momentum tensor:

$$\nabla^\nu \left(R_{\mu\nu} - \frac{1}{2} g_{\mu\nu} R + \Lambda g_{\mu\nu} \right) = 0 \quad \implies \quad \nabla^\nu T_{\mu\nu} = 0, \quad (28)$$

where we have adopted the Einstein convention that there is summation over repeated indices³. Moreover, the semicolon in this equation denotes covariant differentiation with respect to the canonical Levi-Civita connection. A very important consequence of the field equations for the gravitational field is that the local conservation of the energy-momentum tensor implies the equations of motion for the matter fields that contribute to it [27,28,29,30].

Despite the complexity of these equations, they constitute a couple system of second-order non-linear PDEs, a number of exact solutions have been found (see [33] for a very broad account), some of them of great significance like the ones that describe black holes and different large-scale cosmological scenarios. However, these solutions have a high degree of symmetry, representing idealized physical situations where the degrees of freedom of the gravitational field are not turned on.

We mentioned before that Einstein's equations can be divided into constraint and evolution equations. The evolution equations, in certain coordinate gauges and formulated using an appropriate set of variables (combinations of the metric components and its derivatives), constitute a hyperbolic set of partial differential equations that imply that we can set up a well-posed initial value problem for the Einstein field equations. We have also mentioned that the constraints play the role of delimiting the possible initial data, i.e. they select a particular region

³ For instance, for a tensor $A_{\mu\nu}$ we use the notation: $\sum_{\mu=0}^3 A^\mu{}_\mu \equiv A^\mu{}_\mu$.

of the phase space for the dynamics. The hyperbolic structure sets the causality relations through the so-called characteristic surfaces, which in General Relativity are null (i.e. determined by the light cones). Thanks to this, in General Relativity, we cannot construct initial data corresponding to a gravitational wavepacket in which the back of the wavepacket is moving faster than the front, which can lead to shock formation, in contrast to other theories (see, e.g. [34]). This statement may not be valid if we consider the presence of matter fields that by their own dynamics (the characteristic structure of their own evolution equations) generate shock discontinuities, as it is the case of macroscopic fluid descriptions of the matter fields with certain equations of state. Nevertheless, the important point to stress is that in General Relativity, and in vacuum (also in other cases), initial configurations described by smooth initial data will remain smooth under the evolution by strongly hyperbolic formulations of Einstein's equations. In this context, the PSC method is an ideal tool since its convergence properties can be realized in many problems of interest.

More complex problems, with the presence of the dynamics of the true degrees of freedom of the gravitational field (and hence low degree of symmetry), require sophisticated numerical methods to determine the metric tensor and its physical consequences. The collections of the numerical methods, techniques and algorithms to solve Einstein's field equations is an area of research by itself known as Numerical Relativity (see, e.g. [3, 5, 35]). Numerical Relativity is nowadays a mature field in the sense that a number of techniques have been developed for solving different kinds of problems, from cosmology to the emission of gravitational radiation. The focus of this paper is on the subject that inaugurated the field of Numerical Relativity with one of the main results found so far: The finding of critical behaviour in gravitational collapse by Choptuik [36]. In this work we show results on the application of the numerical techniques described above to gravitational collapse in the context of Anti-de Sitter (AdS) spacetimes, which have attracted a lot of attention recently due to its applications to string theory and the gauge-gravity duality. AdS is the maximally symmetric solution of Einstein's equations with a negative cosmological constant (see more in [27]). It has the remarkable property that light rays can reach the AdS boundary in a finite time, in contrast to massive particles which, as in flat spacetime, need an infinite time. This important difference with flat spacetime leads to completely new phenomena and it has important consequences for the study of gravitational collapse.

The dynamics of gravitational collapse in AdS spacetimes demands a very high degree of precision for numerical simulations. This motivated us to first adopt the PSC method as the main discretization tool for our numerical algorithms and later, arbitrary precision computations. This is not the first time that PSC methods have been used in Numerical Relativity, they have successfully been applied to the simulation of the collision of orbiting binary black holes and their emission of gravitational waves [37, 38] (see also e.g. [4, 39, 40, 41, 42]). We have applied these methods to the study of the gravitational collapse of scalar fields in AdS spacetimes and thanks to this we were able to find new relevant physical results [14, 15]. In this section we describe how the PSC method in combination with arbitrary precision is crucial to obtain results that otherwise would not be possible or would be very costly from the computational point of view. We are going to show two different mathematical formulations of the problem of gravitational collapse in AdS spacetime, and also of the evolution of perturbations in AdS spacetime, that lead

to two completely different numerical implementations. We discuss the advantages of each of them in relation to the use of the PSC methods in combination with arbitrary precision.

4.1 Gravitational Collapse

We begin by reviewing the classical problem of gravitational collapse in a flat (Minkowski) spacetime (without cosmological constant, i.e. $\Lambda = 0$). The energy-momentum distribution of the matter collapsing corresponds to a massless real scalar field. For simplicity we assume the spacetime to be spherically symmetric, which means that the Einstein field equations become 1 + 1 PDEs (in time and in the radial direction). Then, the setup of the gravitational dynamics to be followed numerically is quite simple: We consider initial states described by smooth initial data and such that the scalar field distribution is concentrated around a certain radial location. Then, there are only two possible end states for the evolution:

- (i) *Collapse* of the scalar field and the formation of a Black Hole (BH).
- (ii) *Dispersion* of the scalar field with flat spacetime as the end state of the evolution.

To which one of these two states will the evolution drive the system depends on the features of the initial scalar field configuration, in particular on its energy density. An interesting question is what separates these two very different outcomes of the evolution. M. Choptuik [36] carried out a systematic numerical study of this question and found that the dependence of the final state on the initial data is through a single (arbitrary) parameter. Moreover, Choptuik found that in the threshold between collapse and dispersion there is a one-parameter family of critical solutions that exhibit a naked singularity. It was also found that the mass of the collapsed configurations near the threshold exhibits a scaling with a universal exponent. These unexpected results attracted a lot of attention to this problem and constituted a cornerstone in the development of Numerical Relativity. A detailed review of critical gravitational collapse for different types of matter fields and spacetime configurations in General Relativity can be found in [43,44].

In this paper, like in the initial studies by Choptuik, we will restrict ourselves to problems in spherical symmetry. We do not make any further simplification of the problem apart from this one. The first step towards numerical simulations of gravitational collapse is to choose an adequate formulation of the Einstein field equations. We start by choosing what is called a characteristic approach to the problem (introduced in [45,46,47]). The main idea of this approach is to set initial data on a null (or light-like) slice instead of a constant time slice as in a Cauchy-based initial-value problem. The difference is that the normal to a null slice is a light-like one-form while the normal to a constant time slice is a space-like one-form, like in a standard initial-value Cauchy problem. In the context of Numerical Relativity, the main advantage of the characteristic formulation is its ability to approach the BH formation much more efficiently than a typical Cauchy one. In this sense, it is worth mentioning that the initial Choptuik study [36] was based on a Cauchy formulation and used adaptive mesh refinement to reach the necessary

accuracy to obtain the results mentioned above. Later, Garfinkle [47] reviewed the problem by using a characteristic approach and recovered some of the main results without the need of refinement, which shows the power of the characteristic formulation for this type of numerical studies. Our previous studies [14, 15] have also confirmed the superior performance of the characteristic approach by evolving scalar fields, not in asymptotically-flat spacetimes but in Asymptotically-AdS (AAdS) spacetimes (spacetimes whose asymptotic causal structure is the same as the one of AdS). However, the setup we developed in [14, 15] is not suitable for the use of PSC methods so we developed a Finite Differences numerical code. In this section we present a new and improved characteristic scheme that is adapted for the use of the PSC method.

The formulation of the characteristic problem goes as follows: Let us consider a self-gravitating massless scalar field, ϕ . The set of PDEs that we need to solve are the coupled system formed by the Einstein field equations in Eq. (27) and the equations for the scalar field which come from the energy-momentum conservation equations in Eq. (28)]. The energy-momentum tensor for a real massless scalar field is given by

$$T_{\mu\nu} = \phi_{;\mu}\phi_{;\nu} - 2g_{\mu\nu}\phi_{;\alpha}\phi^{;\alpha}, \quad (29)$$

where the covariant derivatives on the scalar field are equivalent to partial derivatives: $\phi_{;\alpha} = \partial\phi/\partial x^\alpha \equiv \phi_{,\alpha}$. Then, the resulting field equation for the scalar field is the well-known Klein-Gordon equation:

$$\square\phi \equiv \phi_{;\mu}{}^{;\mu} = 0. \quad (30)$$

To introduce the characteristic formulation we first need an adapted coordinate system. We choose double-null coordinates for the time-radial section together with spherical coordinates for the spheres of symmetry of the problem. The line element of the spacetime, which is equivalent to specify the metric tensor, in those coordinates is:

$$ds^2 = g_{\mu\nu}dx^\mu dx^\nu = -2f(u, v)r_v(u, v)dudv + r^2(u, v)d\Omega^2, \quad (31)$$

where (u, v) are the double-null coordinates ($\partial/\partial u$ and $\partial/\partial v$ are light-like vectors) and $d\Omega^2 = d\theta^2 + \sin^2\theta d\varphi^2$ is the well-known line element of the unit 2-sphere. Moreover, f and r are two arbitrary functions of (u, v) and r_v is a shorthand for the partial derivative of r with respect to the null coordinate v . The idea of a double-null foliation is to use both directions of propagation of light rays, that is ingoing and outgoing with respect to the radial direction, as part of our system of coordinates. In Figure 11 we show a representation of this idea for the case of an empty (flat) spacetime. In our case, the spacetime is curved by the presence of the massless scalar field ϕ and hence (u, v) would not be perpendicular to the (r, t) coordinate lines.

The set of PDEs for the components of the metric tensor, the metric functions $f(u, v)$ and $r(u, v)$, and the scalar field, $\phi(u, v)$, are obtained by introducing the metric in Eq. (31) into Eqs. (27) and (30). In order to reduce the order of the equations, from second-order to first-order PDEs, and to decouple them we introduce the following new variables associated with the scalar field ϕ (from now on the u

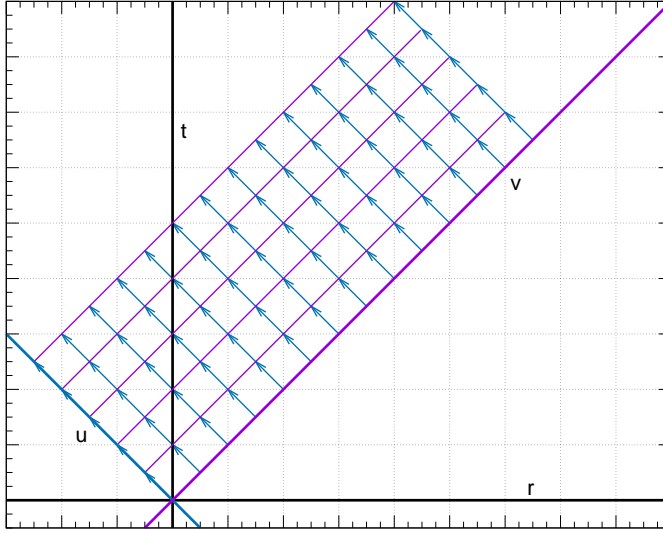


Fig. 11 Scheme of an Evolution using Double-Null Coordinates. The horizontal and vertical lines are the axes corresponding to the time and radial coordinates, (t, r) . In a characteristic problem, we set our initial conditions on a $u = \text{const}$ slide (purple thick line) and evolve each point in the direction indicated by the arrows. This scheme is strictly valid in the case of an empty spacetime where constant null coordinate lines form 45 degrees with respect to the axes (r, t) . In a general case, the (u, v) coordinates will not be straight but the idea is essentially the same.

and v subscripts denote partial differentiation with respect to these coordinates like in r_v):

$$h = \frac{(r\phi)_v}{r_v}, \quad (32)$$

$$\bar{h} = \phi. \quad (33)$$

We also introduce a new metric variable:

$$\bar{f} = -2r_u. \quad (34)$$

With these new variables, the vv and the uv components of the Einstein field equations can be written as:

$$f_v = \frac{f r_v}{r} (h - \bar{h})^2, \quad (35)$$

$$\bar{f}_v = \frac{r_v}{r} (f - \bar{f}). \quad (36)$$

In this characteristic formulation of the initial-value problem we prescribe initial conditions for the variable h on an initial $u = u_i = \text{const}$. null slide, that is $h(u_i, v)$. We also need to prescribe $r(u_i, v)$ and $r_v(u_i, v)$ on that initial null slide. With all

this information we can obtain the rest of variables, at the same null slide $u = u_i$, using the equations above. The expressions for h , f , and \bar{f} are:

$$\bar{h}(u_i, v) = \frac{1}{r} \int_{v_o(u_i)}^v d\tilde{v} h(u_i, \tilde{v}) r_v(u_i, \tilde{v}), \quad (37)$$

$$f(u_i, v) = f(u_i, v_o(u_i)) \exp \left\{ \int_{v_o(u_i)}^v d\tilde{v} \frac{r_v(u_i, \tilde{v})}{r(u_i, \tilde{v})} [h(u_i, \tilde{v}) - \bar{h}(u_i, \tilde{v})]^2 \right\}, \quad (38)$$

$$\bar{f}(u_i, v) = \frac{1}{r} \int_{v_o(u_i)}^v d\tilde{v} f(u_i, \tilde{v}) r_v(u_i, \tilde{v}), \quad (39)$$

where $v_o(u_i)$ and $f(u_i, v_o(u_i))$ are the values of v and $f(u, v)$ respectively, at the origin $r = 0$ on the null slide $u = u_i$. By looking at these expressions we realize that we need to guarantee the regularity of the different quantities at the origin, which translates into imposing the conditions:

$$\bar{h}(u_i, v_o(u_i)) = h(u_i, v_o(u_i)), \quad (40)$$

$$\bar{f}(u_i, v_o(u_i)) = f(u_i, v_o(u_i)). \quad (41)$$

In this way, all the equations have a finite limit when we approach the origin $r = 0$. However, for numerical purposes it is not convenient to have divisions where both numerator and denominator approach zero. This may be particularly problematic in the case of Eq. (39), but we can transform it by using integration by parts and taking the right limits. The result is:

$$\bar{f}(u_i, v) = f(u_i, v) - \frac{1}{r} \int_{v_o(u_i)}^v d\tilde{v} f(u_i, \tilde{v}) r_v(u_i, \tilde{v}) [h(u_i, \tilde{v}) - \bar{h}(u_i, \tilde{v})]^2. \quad (42)$$

Once we have (h, \bar{h}, f, \bar{f}) at the null slide $u = u_i$ we can evolve them to the next null slide by using the evolution equation for the scalar field, i.e. Eq. (30), which comes from the energy-momentum conservation equation (28). At this point, it is important to comment that, due to the spherical symmetry we have imposed on the spacetime and matter fields, only the scalar field has true dynamics since the degrees of freedom of the gravitational field are not activated in spherical symmetry. In other words, there are no gravitational waves present, only scalar field waves. Said that, the evolution equation to pass from a null slide to the next one in our characteristic formulation is given by:

$$h_u = \frac{1}{2r} (f - \bar{f}) (h - \bar{h}). \quad (43)$$

This equation is actually an ODE for each value of v . Indeed, let us consider a particular value of v , say v_* , then Eq. (43) takes the values of the variables at (u_i, v_*) and gives us the value of h at $(u_i + \Delta u, v_*)$, being Δu the time step used in the evolution.

In addition, from Eqs. (34) and (36) we can obtain the evolution equations for r and r_v :

$$r_u = -\frac{1}{2} \bar{f}, \quad (44)$$

$$(r_v)_u = -\frac{1}{2} r_v \left[\frac{f - \bar{f}}{r} \right]. \quad (45)$$

The only missing piece in this characteristic evolution scheme is the value of $f(u_i, v_o(u_i))$ that appears in Eq. (38), which corresponds to the value of f at the origin on the null slide $u = u_i$. This is a freely specifiable quantity that reflects the residual coordinate *gauge* freedom that we have in the choice of the null coordinate v . This, in turn, can be seen as the remaining gauge freedom in completely specifying the radial function r in our characteristic formulation. In particular, it allows us to specify the location of the origin $r = 0$ at the null slides $u = \text{const.}$ Or in other words, the freedom in choosing the motion of the origin ($r = 0$) as we evolve from one null slide to the next one. Indeed, since $r = r(u, v)$, and assuming that $v = v_o(u)$ corresponds to the location of the origin, i.e. $r(u, v_o(u)) = 0$, the equation of motion of the origin as we move through the spacetime foliation in null slides $u = \text{const.}$ is given by:

$$\left. \frac{dv_o(u)}{du} \right|_{v=v_o(u)} = - \left. \frac{r_u}{r_v} \right|_{v=v_o(u)} = \left. \frac{f_o}{2r_v} \right|_{v=v_o(u)}, \quad (46)$$

where we have used Eq. (44). We can then use this freedom to make the origin move, for instance, with a uniform speed. To achieve this we just need to choose the freely specifiable quantity $f(u, v_o(u))$ as:

$$f(u, v_o(u)) = 2 r_v|_{v=v_o(u)} \implies v_o(u) = v_o(u_i) + u. \quad (47)$$

In our formulation the formation of an apparent horizon (AH)⁴ happens when the following condition is fulfilled:

$$r_v \longrightarrow 0, \quad \text{or equivalently,} \quad \frac{\bar{f}}{f} \longrightarrow 0. \quad (48)$$

This limit cannot be reached with our choice of system of coordinates (it corresponds to a coordinate singularity) although we can approach it as much as we want. Then, we assume that an AH has formed when the quantities in the AH condition above reach a value less than 10^{-8} . At that point we stop the simulation.

Finally, in the simulations we have carried out we have used a Gaussian packet as initial data for the scalar field:

$$h(u_i, v) = \epsilon e^{-\frac{(v-b)^2}{\omega^2}}, \quad (49)$$

where the amplitude ϵ , the width ω , and the shift b are the freely specifiable parameters of this 3-parameter family of initial data.

At this point we have presented all the necessary ingredients for the characteristic formulation of the problem. It is well-adapted for its implementation using the PSC method for the discretization in the v coordinate. We evolve from one null slide $u = \text{const.}$ to the next one by using a standard Runge-Kutta 4 (RK4) algorithm. We have implemented this formulation using the PSC method and arbitrary precision tools described in the previous sections. Using the spectral representation, Eq. (67), the error can be estimated from the absolute value of the last spectral coefficient. The value of the coefficients, a_n ($n = 0, \dots, N$), decay

⁴ In general relativity, an apparent horizon is the boundary between light rays that point radially outwards and move outwards, and those directed outward but move inward. Apparent horizons are inside event horizon and hence signal the formation of a BH.

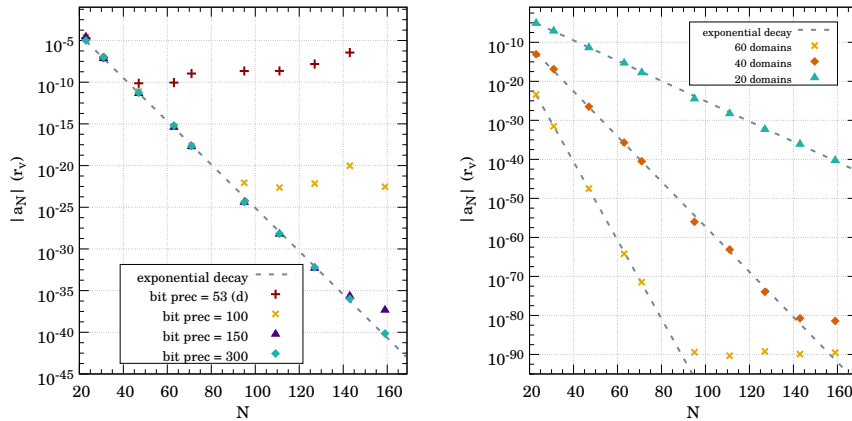


Fig. 12 Convergence in the estimation of the location of the formation of an Apparent Horizon (AH): The left plot shows the truncation error (estimated from the last spectral coefficient) at the moment of AH formation for several different grid configurations, all of them with $D = 20$ subdomains. Each data set corresponds to simulations done with different bit precision. The error decays exponentially (spectral convergence) until the maximum precision is reached. On the right plot we show the impact of adding more subdomains. All sets of data exhibit spectral convergence but the number of subdomains has an impact in the α factor of the exponential decay $e^{-\alpha N}$. These simulations are done with 300 bit precision.

exponentially, reaching or not round-off error. If round-off is not reached, the last spectral coefficient represents an estimation of the truncation error incurred in ignoring the rest of terms in the spectral series. Otherwise, if the last coefficient is the round-off error the last coefficient represents the precision reached. In both cases, it can be used for a good estimation of the error.

We have performed an evolution with the initial data of Eq. (49) and parameters: $\epsilon = 2.00$, $b = 0.15$ and $\omega = 0.05$. This is an example of initial configuration above the critical threshold and hence it will collapse and form an AH. In Figure 12 we show the error in the location of the AH at the end of the evolution in terms of the number of collocation points per subdomain. Since we have different errors at each subdomain, we take the highest of all of them, which corresponds to the subdomain where the collapse takes place. In Figure 12 we only show the error associated with the function r_v , to monitor the first condition in Eq. (48), because is the one that has the highest error of all of the three evolution variables.

Moreover, on the left plot of Figure 12, we use a setup with $D = 20$ subdomains and we change the number of collocation points for different bit precisions. In this plot we have used a log scale in the vertical axis. In all the cases, the error has an exponential decay (spectral convergence) until we reach the precision limit (round-off error) which, of course, improves as we increase the number of bits of our data types. The first one represents a 53 bit precision, equivalent to the standard double precision, which allows us to obtain a maximum accuracy of 10^{-10} - 10^{-11} . Notice that this is few orders of magnitude above the theoretical limit of sixteen digits. This fact is not surprising since we have to consider that during the evolution the numerical noise piles up, reducing the maximum precision. In addition, the number of subdomains used in our test evolutions is not optimal. This

is just a comparison of the same exact setup for several bit precisions. Increasing the number of significant bits we improve the maximum error and with 150 bits (around 45 significant digits) we easily decrease the error up to almost 10^{-40} . On the right plot of Figure 12 we study the influence of the number of subdomains in the error as we change the number of collocation points per subdomain but keeping the number of subdomains constant. The error presents an exponential decay $|\Delta r_v| \approx \exp(-\alpha N)$. Varying the number of subdomains changes the factor of the exponential decay, α . In this case we can reach the minimum error by adding subdomains with less collocation points. This can be a good idea considering that adding subdomains has, in general, a linear impact on the computational time while increasing the number of collocation points, N , has an impact of $\sim N \log N$ or $\sim N^2$ depending on whether the operations in the spectral domain are performed using a FFT transformation or a matrix transformation respectively.

4.2 (In)Stability in Anti-de Sitter Spacetimes

In this section we consider a new physical scenario for the application our hybrid PSC-arbitrary precision method. In the previous section we presented simulations of gravitational collapse, and the eventual formation of an AH, in asymptotically-flat spacetime using a characteristic formulation. In this section, we present results of the evolution of (exact non-linear) “perturbations” in asymptotically Anti-de Sitter spacetimes using a Cauchy formulation of the initial-value problem. Cauchy-type evolutions in spherical symmetry were already done in the study of critical gravitational collapse by Choptuik [36]. In the context of Anti-de Sitter spacetimes they were used recently to study also the problem of critical gravitational collapse in [48]. We adapted this formulation for the use of the PSC method in Refs. [14, 15] and we found new physical features associated with the non-linear evolution. We now present results from a new adaptation of our numerical scheme to include arbitrary precision together with the PSC method.

Anti-de Sitter spacetimes have attracted a lot of attention in the last years, both for the interest in studying the non-linear (in)stability of AdS and for its relevance in the so-called AdS/CFT correspondence (also known as the gauge/gravity duality). As mentioned above, the key feature of AAdS spacetimes is the presence of a boundary that light-like signals (light rays, massless fields, etc.) can reach in a finite time, but such that time-like signals (massive particles, massive fields, etc.) will take infinite proper time to reach. This property changes completely the landscape of gravitational collapse. In the case of a flat spacetime, as it was explained in the previous section, the procedure to study gravitational collapse is to consider an initial profile for the field and then, let it evolve to see whether it collapses forming an AH or, instead, it disperses yielding flat spacetime as the end asymptotic state of the evolution.

The two-case scenario of asymptotically flat spacetimes does not apply to AAdS spacetimes. Indeed, considering an initial profile like in Eq. (49), we can also expect that the dynamics will make this configuration either to collapse [case (i)] or to disperse [case (ii)]. In the case the scalar field configuration collapses it will form a BH that eventually will settle down into a stationary state (a Schwarzschild-Anti-de Sitter BH). However, in the case the scalar field disperses we cannot expect this dispersion to proceed until we reach asymptotically AdS.

The scalar field propagates locally at the speed of light, like light rays, as it follows from the Klein-Gordon equation (30) it satisfies. Then, in some finite time, the scalar field profile will reach the AdS boundary, it will bounce back and will try to collapse again, only that the non-linear evolution would have changed the profile and we will be in the initial situation but with different initial conditions. Therefore, there will be again two possible outcomes, collapse to form an AH or dispersion until reaching the AdS boundary in a finite time and bounce back. This process will repeat itself until the scalar field configuration will have a profile dense enough to finally collapse forming an AH. Then, the possible states of the evolution of a scalar profile in spherically-symmetric AAdS spacetimes are:

- (1) *Direct Collapse* of the scalar field and the formation of a Black Hole (BH).
- (2) *Collapse* of the scalar field and BH formation after 1 bounce off the AdS boundary.
- ⋮
- (n_c) *Collapse* of the scalar field and BH formation after $n_c - 1$ bounces off the AdS boundary.

During the trip to the AdS boundary and back, the non-linear character of relativistic gravitation acts and there is an energy transfer from low frequency (long wavelength) modes towards high frequency (short wavelength) modes, similar to what happens in the onset of turbulence. Due to this analogy, this process, that at some point will end in the collapse of the scalar field profile, has been named the *turbulent instability* of AdS spacetime. That is, no matter how small would be the amplitude of the initial profile (perturbation), the field will finally collapse and the end state would be an AdS-BH spacetime. Nevertheless, although this turbulent instability may appear to be a generic feature of the dynamics in AdS spacetime, there are indications of the existence of some islands of stability (see, e.g. [49] and references therein) that will not follow the channels just described. The reason is that some stable configurations have been found for some forms of initial configurations, but the exact extend of these “stability islands” in the parameter space of initial configurations is still under debate. In order to study this question we need extremely long and accurate evolutions. In summary, the end state of the evolution of perturbations in AdS spacetimes is an ideal testbed for numerical techniques that provide high accuracy, beyond the standard one, as the problem is highly demanding. In order to illustrate this, in this section we present a test case in which we evolve an initial massless scalar field configuration in AAdS spacetimes during two of these bounces and compare the accuracy obtained using double precision with the one using 300-bit precision.

In order to solve the Einstein field equations [Eq. (27)] coupled to the massless scalar field equation [Eq. (30)] in this new scenario we need a different coordinate system. This coordinate system has to be adapted to a Cauchy-type initial-value problem and, at the same time, it has to incorporate the AdS asymptotic structure of the spacetime. With this in mind, the form of the spacetime line element that

we consider is:

$$ds^2 = g_{\mu\nu} dx^\mu dx^\nu = \frac{\ell^2}{\cos^2 x} \left(-Ae^{-2\delta} dt^2 + \frac{dx^2}{A} + \sin^2 x d\Omega^2 \right), \quad (50)$$

where $A = A(t, x)$ and $\delta = \delta(t, x)$ are two arbitrary metric functions, t is the time coordinate, and x is a compactified radial coordinate in such a way that the AdS boundary is located at $x = \pi/2$ instead of at infinity. The overall factor contains ℓ , the AdS length scale, which is related to the negative cosmological constant of the spacetime, $\Lambda < 0$ [see Eq. (27)], by the expression: $\ell^2 = -3/\Lambda$. The time coordinate t has an infinite range, i.e. $t \in (-\infty, \infty)$, whereas x , being compactified, goes from $x = 0$ (center) to $\pi/2$ (AdS boundary). We can recover AdS spacetime by setting $A = 1$ and $\delta = 0$.

Again, the system of PDEs that we obtain, by choosing the right combination of variables, can be reduced to a first-order system of PDEs that can be shown to be strongly hyperbolic. In addition, in order to use our multidomain scheme, we can further specialize our variables and take them to be the eigenfields of this hyperbolic system, also known as the characteristic variables (see Refs. [19, 15] for a proper definition and an exact derivation for our case). The form of the characteristic variables associated with the scalar field that we adopt is:

$$U = \frac{1}{\cos x} \left(\phi_x - \frac{e^\delta}{A} \phi_t \right), \quad (51)$$

$$V = \frac{1}{\cos x} \left(\phi_x + \frac{e^\delta}{A} \phi_t \right), \quad (52)$$

where again, the (t, x) subscripts denote partial differentiation with respect to these coordinates. Then, using the (t, x) coordinates and the (U, V) variables, the evolution problem is reduced to the following coupled system of PDEs:

$$U_t = -Ae^{-\delta} U_x - \frac{(3 - 2 \cos^2 x)}{\sin x \cos x} U e^{-\delta} (1 - A) - \frac{Ae^{-\delta}}{\sin x \cos x} (U + V) + \frac{\sin x}{\cos x} U Ae^{-\delta}, \quad (53)$$

$$V_t = +Ae^{-\delta} V_x + \frac{(3 - 2 \cos^2 x)}{\sin x \cos x} V e^{-\delta} (1 - A) + \frac{Ae^{-\delta}}{\sin x \cos x} (U + V) - \frac{\sin x}{\cos x} V Ae^{-\delta}. \quad (54)$$

It is also convenient to introduce the following normalized variable associated with the scalar field:

$$\psi = \frac{\phi}{\cos^2 x}. \quad (55)$$

This new scalar field variable satisfies both an evolution equation

$$\psi_t = \frac{Ae^{-\delta}}{2 \cos x} (V - U), \quad (56)$$

and also a constraint equation (one that does not contain time derivatives, only spatial derivatives):

$$\psi_x = 2 \frac{\sin x}{\cos x} \psi + \frac{1}{2} \frac{U + V}{\cos x}. \quad (57)$$

Then, we can solve for ψ either by evolving Eq. (56) or by solving this constraint equation on a constant time slice. Regarding the metric functions, as we mentioned above, we do not expect to have hyperbolic equations for them since in spherical symmetry the true gravitational degrees of freedom are turned off. Indeed, we only obtain constraint equations for both δ and A :

$$\delta_x = -\frac{1}{2} \sin x \cos^3 x (V^2 + U^2), \quad (58)$$

$$A_x = \frac{1 + 2 \sin^2 x}{\sin x \cos x} (1 - A) - \frac{A}{2} \sin x \cos^3 x (V^2 + U^2), \quad (59)$$

from which $\delta(t, x)$ and $A(t, x)$ can be obtained at a given time, once we have the solution for (U, V) via the evolution equations, by performing the following integrals:

$$\delta(t, x) = \int_x^{\pi/2} dy \sin y \cos^3 y \left(\frac{U^2 + V^2}{2} \right), \quad (60)$$

$$A(t, x) - 1 = -\frac{\cos^3 x e^\delta}{\sin x} \int_0^x dy e^{-\delta} \sin^2 y \left(\frac{U^2 + V^2}{2} \right), \quad (61)$$

where the boundary conditions are $A = 1$ both at $x = 0$ and $x = \pi/2$ and we have chosen $\delta(\pi/2) = 0$, fixing the time coordinate t as the proper time at the AdS boundary. Then, the Cauchy evolution goes as follows: (i) We prescribe initial data on an initial Cauchy surface $t = t_o = \text{const.}$ for (U, V) , i.e. $U(t_o, x)$ and $V(t_o, x)$. (ii) Using equations (57), (60), and (61) we find $\psi(t_o, x)$, $\delta(t_o, x)$ and $A(t_o, x)$. (iii) With this information we evolve (U, V) from t_o to $t_o + \Delta t$ using the evolution equations (53) and (54) and the boundary conditions. In our numerical simulations we have considered the following family of Cauchy initial data:

$$U(t_o, x) = \epsilon \exp\left(-\frac{4 \tan^2 x}{\pi^2 \sigma^2}\right), \quad (62)$$

$$V(t_o, x) = -U(t_o, x), \quad (63)$$

where the freely specifiable parameters ϵ and σ (amplitude and width of the Gaussian profile respectively) are chosen to be: $\epsilon = 2.0$ and $\sigma = 0.4$.

We set up a multidomain grid with $D = 10$ subdomains and we change the number of collocation points per subdomain to see how the error changes for both double precision and for 300-bit precision. We evolve the initial ‘‘perturbation’’ for the time corresponding to two bounces off the AdS boundary. Since we need very high accuracy, we have used a sixth-order Runge-Kutta 10,6(7) (see Refs. [50, 51] for details). This ODE solver uses ten intermediate steps to generate a sixth-order accurate in time integration with a seventh-order step that is used as an estimation of the error.

At any time step, we can compute the energy contained inside a sphere of a given compactified radius x , which is known as the mass function:

$$\mathcal{M}(t, x) = e^\delta \int_0^x dy e^{-\delta} \sin^2 y \left(\frac{U^2 + V^2}{2} \right), \quad (64)$$

so that the total energy contained in the spacetime is $M(t) = \mathcal{M}(t, \pi/2)$. Using General Relativity it is possible to show that $M(t)$ should not depend on time, i.e.

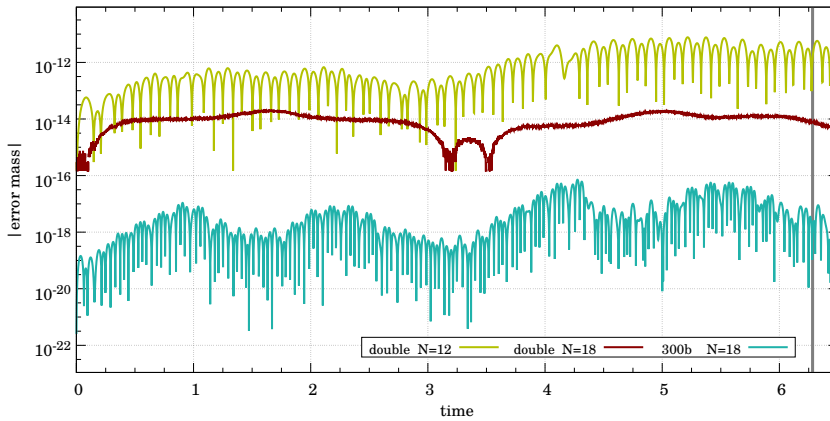


Fig. 13 Evolution of the Mass Error Function in AAdS Spacetimes. We compare three different grid/precision configurations with $D = 10$ subdomains. Using double precision, the use of $N = 18$ collocation points per subdomain (red line) is enough to reach the round-off error. The same number of collocation points but with 300-bit precision (turquoise line) allows us to reduce a few orders of magnitude the error during the evolution. It is interesting to notice how, when the error is determined by the discretization error, several fluctuations are present while in the case dominated by machine round-off the error remains almost flat during the time evolution. The grey vertical line to the right shows the instant of time at which we measure the error for the study presented in Figure 14.

it is a conserved quantity. Then, we can monitor the conservation of M as indicator of the accuracy of the simulation. To that end we introduce the following mass error function:

$$\Delta M(t) = \frac{|M(t) - M(t_o)|}{M(t_o)}. \quad (65)$$

We have performed a set of numerical evolutions to assess the relevance of arbitrary precision in these computations. In Figure 13 we show the evolution of the mass error function of Eq. (65). The purple line shows an evolution with a low number of collocation points ($N = 12$) and with double precision. The error oscillates in the range $10^{-12} - 10^{-11}$. Increasing the number of collocation points to $N = 18$ (red line in Figure 13) we can decrease the mass error down to around 10^{-14} . It is interesting to notice the different behaviour between these two lines. In the first case, there is plenty of oscillations and we estimate the error by taking the maximum value. This is due to the fact that here the error is determined by the discretization error in such a way that the total error can oscillate between the discretization and the round-off errors. In the second case we have reached by far the round-off error and the profile is quite flat. Then, it is obvious that it cannot be improved by using double precision. Just changing from double precision to 300-bit precision but with the same number of collocation points per subdomain, the error drops more than two orders of magnitude and, again, it is determined by the discretization.

Once the massless scalar field configuration has bounced twice off the AdS boundary and has come back to the initial location ($t \approx 2\pi$), we have studied not only the error mass function at that moment, but also the error in the charac-

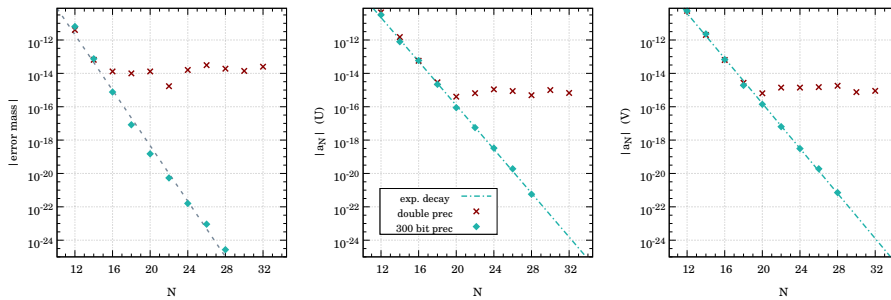


Fig. 14 Convergence of the Truncation Error in Evolutions in AdS Spacetimes. The figure shows the error in an AdS spacetime evolution using double (red dots) and 300-bit (turquoise dots) precision computations. The plots represent the normalised mass error ΔM (left), the truncation error for U (centre), and the truncation error for V (right) with respect to the number of collocation points per subdomain N . This information is taken at the same time ($t = 2\pi$) after the massless scalar field configuration has bounced twice off the AdS boundary. All the simulations use $D = 10$ subdomains.

teristic fields U and V . To that end, we have used the absolute value of the last spectral coefficient in the subdomain where the error is maximum. This is shown in Figure 14 for configurations with $D = 10$ subdomains and for different number of collocation points and numerical precisions. As expected, the error in the three quantities [ΔM (left plot), U (center plot), and V (right plot)] decays exponentially until we reach round-off error. For double precision (red points) this happens at values of the order of $\sim 10^{-14} - 10^{-15}$. This is easily improved when we use higher-order precision, as in the case shown with turquoise dots in the same figure. This corresponds to 300-bit precision and allows us to evolve the scalar field profile with an accuracy below 10^{-24} with a number of collocation points per subdomain as small as $N = 28$, for a total of $(N + 1)D = 290$ collocation points.

5 Conclusions and Future Perspectives

In this paper we have shown the potential of the combination of Pseudo-Spectral Collocation methods and arbitrary-precision arithmetics for the solution of ordinary/partial differential equations, and more specifically for hyperbolic problems related to the description of gravitational collapse in relativistic gravitation. The exponential convergence of the PSC method makes it a very suitable choice for reaching the maximum accuracy associated with a certain bit precision with a relatively low number of discretization (collocation) points as compared with other techniques. In this sense, we have seen that the power-law convergence of finite difference algorithms makes it unfeasible to reach the needed accuracy within a reasonable number of discretization points. In addition, the PSC method does not require relevant changes in the algorithms as we increase the number of precision bits, in contrast with finite difference algorithms, where we need to adapt the algorithm so that the error scales in a way that we can reach the level of accuracy allowed by the choice of precision arithmetics.

In Sec. 3.3, we have seen that the main problem of arbitrary precision arithmetics is that it is usually implemented via a software layer that slows down significantly the computations with respect to the speed of standard double precision arithmetics. In this sense, the PSC method helps since the number of collocation points required is relatively small and therefore, although the sparsity of the matrices involved in certain algorithms can be a drawback. Moreover, the multidomain scheme proposed in this paper allows for a simple parallelization of the computations, as we have shown with the use of OpenMP in our examples. We have also shown that the scalability of the multidomain scheme is close to the ideal case of full parallelism. Nevertheless, it would be desirable to explore improvements in the computation speed (and cost) based on an exploration of a more low-level approach to arbitrary precision arithmetics.

All the numerical examples and experiments reported in this paper have been carried out using a new library, the **ANETO** library [13], that we have developed in the course of our numerical studies of gravitational collapse in the context of General Relativity. The current version has been released with a few basic tools to deal with evolution problems but it can be extended in the future to include other tools that the PSC methods offers. In this sense, one of the main possible improvements would be to add a solver for linear ODEs and also the incorporation of tools for non-linear systems. In addition, it would be interesting to add some type of Adapting Mesh Refinement to allow the grid to be more flexible under different conditions. At the moment the library, like the systems analyzed in this work, can only deal with evolution problems in just one spatial dimension. It would be desirable to change in a future in order to incorporate tools to work on higher dimensional problems. Another aspect that we have not discussed much in this paper is the question of time integration. As the demand for accuracy increases, this aspect becomes more and more important and then, high-order integration algorithms would be required both in relation to the accuracy provided by the PSC method and to the one provided by arbitrary-precision arithmetics, otherwise we may be in a situation in which the evolution takes a considerably large number of time steps. An interesting solution to improve the accuracy of the evolutions with arbitrary precision arithmetics could be a spectral time integration like the one proposed in Refs. [52,53,41].

Acknowledgements

The authors acknowledge the high-performance computing resources provided by the Consorci de Serveis Universitaris de Catalunya (CSUC) and the Galicia Supercomputing Center (CESGA) under projects ICTS-CESGA-249 and ICTS-CESGA-266. They also acknowledge support from contracts ESP2013-47637-P, ESP2015-67234-P, and ESP2017-90084-P (Spanish Ministry of Economy and Competitiveness of Spain, MINECO). DS acknowledges support from a FPI doctoral contract BES-2012-057909 from MINECO.

A Basic Elements of the PSC Method

In this Appendix we include some technical details that are relevant to understand our use of the PSC method in this work.

A.1 The PSC Grid

In this work we use the Chebyshev polynomials and a Lobatto-Chebyshev grid. The spectral coordinates, $X \in [-1, +1]$, of the collocation points are:

$$X_i = -\cos\left(\frac{\pi i}{N}\right) \quad (i = 0, 1, \dots, N), \quad (66)$$

which includes the two boundary points, $X = -1$ and $X = 1$.

A.2 The Spectral and the Physical Representations

In the PSC method there two ways of representing the approximation to our unknowns: (i) The *spectral* representation [see also Eq. (2)]:

$$\mathbf{u}_N(t, x) = \sum_{n=0}^N \mathbf{a}_n(t) T_n(X), \quad (67)$$

where a mapping between the physical coordinate x and the spectral one X , $x = x(X)$ is assumed. (ii) The *physical* representation:

$$\mathbf{u}_N(t, x) = \sum_{i=0}^N \mathbf{u}_i(t) C_i(X), \quad (68)$$

where $\mathbf{u}_i(t)$ are the values of our variables \mathbf{u} at the collocation point X_i , and $\{C_j(X)\}_{j=0, \dots, N}$ are the *cardinal* functions [17], which have the properties: $C_i(X_j) = \delta_{ij}$ ($\forall i, j = 0, \dots, N$). In the case of the Lobatto-Chebyshev collocation grid, the cardinal functions are:

$$C_i(X) = \frac{(1 - X^2)T'_N(X)}{(1 - X_i^2)(X - X_i)T''_N(X_i)} \quad (i = 0, \dots, N). \quad (69)$$

These two representation can be related via a matrix transformation:

$$\mathbf{u}_i = \sum_{n=0}^N \mathbb{M}_{in} \mathbf{a}_n, \quad \mathbb{M}_{in} = T_n(X_i) \quad (i, n = 0, \dots, N). \quad (70)$$

When, as in our case, the basis functions are orthogonal polynomials associated with a Sturm-Liouville problem, they also have a discrete scalar product associated with the Gaussian quadratures of the collocation grid [17]:

$$[T_n, T_m] = \sum_{i=0}^N w_i T_n(X_i) T_m(X_i) = \delta_{nm} \nu_n^2, \quad (71)$$

where w_i are the weights and the constants ν_n^2 determine the norm of the orthogonal polynomials:

$$w_i = \frac{\pi}{N \bar{c}_i}, \quad \nu_n^2 = \frac{\pi \bar{c}_n}{2} \quad (\bar{c}_n = 2 \text{ if } n = 0 \text{ or } n = N \text{ and } \bar{c}_n = 1 \text{ otherwise}). \quad (72)$$

Using this, the inverse transformation between representations is:

$$\mathbf{a}_n = \frac{[\mathbf{u}_N, T_m]}{[T_n, T_n]} = \frac{1}{\nu_n^2} \sum_{i=0}^N w_i T_n(X_i) \mathbf{u}_i = \sum_{i=0}^N \mathbb{M}_{ni}^{-1} \mathbf{u}_i, \quad \mathbb{M}_{ni}^{-1} = \frac{T_n(X_i) w_i}{\nu_n^2}. \quad (73)$$

Introducing a new coordinate via $X = \cos \theta$ ($\theta \in [0, \pi]$), the series in Chebyshev polynomials [Eq. (3)] becomes a cosine series since $T_n(\cos \theta) = \cos(n\theta)$. In the particular case of the Lobatto-Chebyshev grid [Eq. (66)], the components of the matrix transformation in Eq. (70) become: $\mathbb{M}_{in} = T_n(X_i) = (-1)^n \cos(n i \pi / N)$. The resulting transformation becomes then a Discrete Cosine Transform (DCT) that can be computed by using a $2N$ Fast Fourier Transform (FFT) algorithm whose computation cost scales as $\sim N \ln N$ with the number of collocation points [16, 17] in contrast with the $\sim N^2$ scaling of the matrix transformation.

A.3 Mappings between the Spectral and the Physical Coordinates

Let us assume that the *physical* coordinate x takes values in the interval $\Omega = [x_L, x_R]$, where x_L and x_R are the boundary points of the physical domain. The probably most common mapping to the spectral coordinate X ($X \in [-1, 1]$) is the linear mapping:

$$X \longrightarrow x(X) = \frac{x_R - x_L}{2} X + \frac{x_L + x_R}{2}, \quad (74)$$

The distribution (density) of the grid points in x is the same as the distribution of collocation points in X . There are situations where the accumulation of collocation points near the boundaries puts stringent constraints on the Courant-Friedrichs-Lewy (CFL) condition for the stability of the evolution of PDEs (see, e.g. [54]). In the case of the PSC method, the CFL condition takes the form $\Delta t < C N^{-2}$ (where C is a certain constant), in contrast with the typical form for standard finite-difference schemes for PDEs, where $\Delta t < C' N^{-1}$ (where C' is another constant). We can use the mapping $x(X)$ to change the distribution of points in the physical space and improve the CFL condition. We can also use the $x(X)$ mapping for mesh refinement. From a general perspective, any reasonable mapping can be used as long as it is smooth enough and has a non-vanishing derivative in the coordinate range considered [55]. We give here two examples of alternative mappings. First, one that mimics a uniform grid in x :

$$X \longrightarrow x(X) = \gamma + \beta \frac{\arcsin(\alpha X)}{\arcsin(\alpha)}, \quad (75)$$

where the uniformity in the separation of the points is controlled by the parameter α . Setting it to one makes the grid exactly uniform but singular. This can be avoided by taking $\alpha = 1 - \epsilon$ with ϵ very small. This reproduces an almost uniform grid without any singularity. By setting this parameter to zero, we recover the Lobatto-Chebyshev grid. The range of the coordinate x can be controlled with the constants β and γ . This mapping was introduced by Kosloff and Tal-Ezer [56] in order to recover a CFL condition of the type $\Delta t \sim O(N^{-1})$. The second example of mapping accumulates grid points near only one of the two boundaries and is based on a simple exponential function:

$$X \longrightarrow x(X) = \gamma + \beta e^{\alpha(1+X)}, \quad (76)$$

where, again, β and γ determine the range of the coordinate x and α controls how strong is the accumulation of grid points near the left boundary of x . A graphical representation of the three mappings in Eqs. (74), (75) and (76) is shown in Figure 1.

A.4 Differentiation, integration and filtering

The computation of derivatives can be fully performed in the physical representation by using a matrix transformation that involves all the values of our variables in the collocation grid. Indeed, from Eq. (68)

$$\frac{\partial \mathbf{u}}{\partial x} = \sum_{i=0}^N \mathbf{u}_i(t) \frac{dX(x)}{dx} \frac{d\mathcal{C}_i(X)}{dX} \Rightarrow (\partial_x \mathbf{u})_k = \sum_{i=0}^N \mathbf{u}_i(t) \left(\frac{dX(x)}{dx} \right)_{X_k} \left(\frac{d\mathcal{C}_i(X)}{dX} \right)_{X_k}, \quad (77)$$

where the subscript X_k denotes evaluation at the collocation point $X = X_k$. In matrix form

$$(\partial_x \mathbf{u})_i = \sum_{k=0}^N \mathbb{C}_{ik} \mathbf{u}_k, \quad \mathbb{C}_{ik} = \left(\frac{dX(x)}{dx} \right)_{X_k} \left(\frac{d\mathcal{C}_i(X)}{dX} \right)_{X_k} \quad (i, k = 0, \dots, N). \quad (78)$$

This is an order $\sim N^2$ operation. A less expensive alternative is to carry out differentiation in the spectral space. For our choice of PSC method, the spectral coefficients of the derivatives, \mathbf{b}_n , in terms of the spectral coefficients of the variable, \mathbf{a}_n , are given by the following

algorithm [17, 16]:

$$\begin{cases} \mathbf{b}_N = 0, \\ \mathbf{b}_{N-1} = 2N\mathbf{a}_N, \\ \mathbf{b}_n = \frac{1}{\bar{c}_n} [2(n+1)\mathbf{a}_{n+1} + \mathbf{b}_{n+2}] \quad (n = N-2 \dots 0), \end{cases} \quad (79)$$

where the \bar{c}_n are given in Eq. (72). Then, the scheme for differentiation in our Chebyshev PSC method is:

$$\partial_x : \{\mathbf{u}_i\} \xrightarrow{\text{DCT}} \{\mathbf{a}_n\} \xrightarrow{\tilde{\partial}_x} \{\mathbf{b}_n\} \xrightarrow{\text{DCT}} \{(\partial_x \mathbf{u})_i\}, \quad (80)$$

where $\tilde{\partial}_x$ is the spectral-space derivative operator whose action is given in Eq. (79). The computational cost of differentiation, using the DCT transform for changing representation, scales as $\sim N \log N$.

In the case of integration, there are different operators we are going to be interested in. First, let us consider the following simple first-order ODE

$$\frac{df(x)}{dx} = g(x), \quad (81)$$

with a boundary condition at $x = x_0$, $f(x_0) = f_0$. The solution is simply given by

$$f(x) = f_0 + \int_{x_0}^x dx' g(x'). \quad (82)$$

This is what we call *integration from the left* because it incorporates a (boundary) condition at $X = X_- = -1$ (assuming a mapping $x = x(X)$ so that $x_0 = x(X_-)$):

$$I_L(x(X)) = I_L(x_0) + \int_{X_-}^X dX' \left(\frac{dx}{dX} \right)_{X'} g(X'), \quad (83)$$

where $I_L(x_0) = f_0$. The scheme for the full left-integration process is:

$$\int_{X_-}^X : \{\mathbf{u}_i\} \xrightarrow{\text{DCT}} \{\mathbf{a}_n\} \xrightarrow{\int_L} \{\mathbf{b}_n^L\} \xrightarrow{\text{DCT}} \{(\int_{X_-}^X \mathbf{u})_i\}, \quad (84)$$

where $\{\mathbf{b}_n^L\}$ are the spectral coefficients corresponding to the integral $I_L(x(X))$. The relation with the spectral coefficients of the variables \mathbf{u} , $\{\mathbf{a}_n\}$, which defines the operator denoted by \int_L in Eq. (84), are given by:

$$\begin{cases} \mathbf{b}_N^L = \frac{\mathbf{a}_{N-1}}{2N}, \\ \mathbf{b}_n^L = \frac{1}{2n} (\bar{c}_{n-1} \mathbf{a}_{n-1} - \mathbf{a}_{n+1}) \quad (n = N-1, \dots, 1), \\ \mathbf{b}_0^L = I(x(X_-)) - \sum_{n=1}^N (-1)^n \mathbf{b}_n. \end{cases} \quad (85)$$

In the same way, we can introduce the right integration (the boundary condition is imposed at the right boundary, i.e. at $X = X_+ = +1$):

$$I_R(x(X)) = I_R(x_0) + \int_X^{X_+} dX' \left(\frac{dx}{dX} \right)_{X'} g(X'). \quad (86)$$

The scheme for the full right-integration process is:

$$\int_X^{X_+} : \{\mathbf{u}_i\} \xrightarrow{\text{DCT}} \{\mathbf{a}_n\} \xrightarrow{\int_R} \{\mathbf{b}_n^R\} \xrightarrow{\text{DCT}} \{(\int_X^{X_+} \mathbf{u})_i\}. \quad (87)$$

The action of the operator $\int_{\mathbb{R}}$ on the spectral coefficients of our variables, $\{\mathbf{a}_n\}$, is given by

$$\begin{cases} \mathbf{b}_N^{\mathbb{R}} = -\frac{1}{2N}\mathbf{a}_{N-1}, \\ \mathbf{b}_n^{\mathbb{R}} = -\frac{1}{2n}(c_{n-1}\mathbf{a}_{n-1} - \mathbf{a}_{n+1}) & (n = N-1, \dots, 1), \\ \mathbf{b}_0^{\mathbb{R}} = I_{\mathbb{R}}(x(X_+)) - \sum_{n=1}^N \mathbf{b}_n^{\mathbb{R}}. \end{cases} \quad (88)$$

Finally, let us consider the following second-order linear ODE:

$$\alpha_2(X) \frac{d^2 f(X)}{dX^2} + \alpha_1(X) \frac{df(X)}{dX} + \alpha_0(X) f(X) = S(X). \quad (89)$$

Once we discretize it with the PSC method we are left with the linear algebra problem:

$$\sum_{j=0}^N \left[\alpha_2^i \mathcal{D}_{XX}^{ij} + \alpha_1^i \mathcal{D}_X^{ij} + \alpha_0^i(X) \mathbb{I}^{ij} \right] \mathbf{f}^j = \mathbf{S}^i, \quad (90)$$

where the $N+1$ vectors α_0 , α_1 , α_2 , \mathbf{f} , and \mathbf{S} contain the collocation values of the functions $\alpha_0(X)$, $\alpha_1(X)$, $\alpha_2(X)$, $f(X)$, and $S(X)$ respectively; \mathbb{I} denotes the $(N+1) \times (N+1)$ identity matrix; \mathcal{D}_X^{ij} , the matrix associated with the first-order differential operator d/dX ; and \mathcal{D}_{XX}^{ij} the matrix associated with the second-order one, d^2/dX^2 . Although the matrix in this expression is sparse, the compression property of the PSC method makes the value of N to be in general much smaller than in other numerical methods and thus, the computational cost is quite reasonable. Here, a multidomain decomposition would reduce the sparsity of the matrix. For a general ODE, assuming the highest-order derivative is of order O , we can generalize the form of the linear problem in Eq. (90) to the simple form:

$$\sum_{j=0}^N \mathcal{O}^{ij} \mathbf{f}^j = \sum_{k=1}^O \sum_{j=0}^N \left[\alpha_k^i \mathcal{D}_{(k)}^{ij} \right] \mathbf{f}^j = \mathbf{S}^i, \quad (91)$$

where we have adopted the following conventions: $\mathcal{D}_{(0)}^{ij} = \mathbb{I}^{ij}$, $\mathcal{D}_{(1)}^{ij} = \mathcal{D}_X^{ij}$, and $\mathcal{D}_{(2)}^{ij} = \mathcal{D}_{XX}^{ij}$, and in general $\mathcal{D}_{(k)}^{ij}$ is the matrix associated with the differential operator d^k/dX^k . The first-order differentiation matrix, $\mathcal{D}_{(1)}^{ij}$, is given by (see, e.g. [17]):

$$\mathcal{D}_{(1)}^{ij} = \begin{cases} \frac{\bar{c}_i}{\bar{c}_j} \frac{(-1)^{i+j}}{X_i - X_j} & i \neq j, \\ -\frac{X_i}{2(1-X_i^2)} & 1 \leq i = j \leq N-1, \\ \frac{2N^2+1}{6} & i = j = 0, \\ -\frac{2N^2+1}{6} & i = j = N, \end{cases} \quad (92)$$

and higher-order differentiation matrices (see, e.g. [57]) are obtained from the first-order one as follows

$$\mathcal{D}_{(k)}^{ij} = \left(\mathcal{D}_{(1)}^k \right)^{ij} = \left(\mathcal{D}_{(1)} \times \overset{k}{\dots} \times \mathcal{D}_{(1)} \right)^{ij}. \quad (93)$$

In the linear case the problem is solved after inverting the associated matrix. In the case of non-linear ODEs, the system cannot be directly inverted and we have to resort to iterative methods.

The final topic of this section is filtering. In evolution problems, numerical noise usually originates as low-amplitude high-frequency modes that eventually pile up along the numerical evolution, sometimes making the algorithm unstable and, in many cases, preventing us from obtaining an accurate solution. In the spectral representation, these high-frequency modes can be identified and eliminated by applying a filter. The filter has to be carefully chosen in order

to avoid eliminating modes that contain part of the solution to our problem, but in general, as Figure 67 shows, these modes are usually at the level of round-off error and we can eliminate them without altering the real content of the solution. For our vector of variables, \mathbf{u} , the filtering scheme (with associated filter σ) is:

$$\sigma : \{\mathbf{u}_i\} \xrightarrow{\text{DCT}} \{\mathbf{a}_n\} \xrightarrow{\sigma} \{\mathbf{a}_n^\sigma\} = \left\{ \sigma \left(\frac{n}{N} \right) \mathbf{a}_n \right\} \xrightarrow{\text{DCT}} \{\mathbf{u}_i^\sigma\}. \quad (94)$$

A frequently used filter is the exponential filter:

$$\sigma(\eta) = \exp\{-\alpha \eta^\gamma\}, \quad (95)$$

where α and γ are freely specifiable parameters of the filter. The parameter α is usually fixed to $\alpha = -\log \varepsilon_M$, where ε_M represents the machine accuracy ($\alpha \approx 36.0437$ for double precision). The typical values of γ that we have used are of the order of $\sim (9/5)N$.

B The ANETO Library

The Arbitrary precision solvEr with pseudo-specTral MethOds (**ANETO**) library is a platform to use the PSC method to solve differential equations using arbitrary precision arithmetic. **ANETO** has been released as Free Software under a GNU General Public License (GPL) and it can be found in [13], including source code and full documentation of the classes and functions available as well as examples of its functionalities. The library was originally developed due to need to go beyond the standard double precision for the study of certain problems associated with gravitational collapse in the context of the General Theory of Relativity. We have used the library in this paper to show the great potential of combining the PSC method with arbitrary precision arithmetic.

The library has been developed using C++ templates, which allows for the use of any kind of data type. In several of the computations done for this paper, we have used standard types like **float** and **double** for single and double precision respectively. For the **quadruple precision** type we have used the **float128** type implemented in the Boost Multiprecision library [58]. For general bit precision, we have used the GNU's Multiple Precision Floating-Point Reliable (MPFR) Library [59], a C library for multiple-precision floating-point computations with correct rounding, with a C++ wrapper [60] as an interface.

The tools of the library are distributed in two different C++ classes following the structure described in Sec. 2. The first class is **spectral_grid<>** and generates an individual Lobatto-Chebyshev collocation grid. The second class is **multidomain<>** and generates a multidomain structure where each subdomain is a single Lobatto-Chebyshev collocation grid. In this appendix we briefly explain the main details of how these classes are implemented in the **ANETO** library.

B.1 Class Spectral Domain

The class **spectral_grid<>** generates a *Lobatto-Chebyshev* collocation grid defined on the *spectral* interval $X = [-1, 1]$ of $N + 1$ points [see Eq. (66) for the location of the collocation points]. We can then define functions on this interval which are fully characterized by their values at the collocations points of the grid, what we named as the *physical* representation of a function. In general, the information associated with any given function is stored using this representation but, quite frequently, some important operations are performed using the *spectral* representation, that is, the coefficients of the expansion in Chebyshev polynomials [see Eq. (67)]. The class **spectral_grid<>** makes the transformation between the two representations using a discrete cosine transformation (DCT). The library can carry out this transformation either through a matrix transformation, in that case the number of operations scales as $\sim N^2$, or using a Fast Fourier algorithm (FFT), in which case the number of operations scales as $\sim N \log N$. The FFT algorithm that the library used comes from the Eigen library [61], which is optimised for the case in which the number of points is a power of two and therefore, the recommended use (i.e. the default one), is to use the FFT in those cases and the matrix transformation in the rest.

This class can perform several types of operations on a Lobatto-Chebyshev grid, like for instance indefinite integrals. In that case, it distinguishes integration starting from the left boundary, $X_- = -1$, from integration starting from the right boundary, $X_+ = +1$. In the case of integration from the left, the operation is denoted by $I_L(X; \{f_i\}, I_-)$, where X is the any value in the spectral interval, $\{f_i\}$ ($i = 0, \dots, N$) are the collocation values of the integrand function and I_- is a boundary condition on the left boundary of the spectral integral. Then, the operation I_L returns the values at the collocation points of the accumulative integral compute from the left boundary, $X_- = -1$, given the boundary condition specified precisely by I_- . And the analogous operation can be introduced for indefinite integration from the right, which we denote by $I_R(X; \{f_i\}, I_+)$, where the only difference is that now we have to specify a boundary condition on the right boundary, $X_+ = 1$, that is, I_+ . The exact expressions and details are given in Eqs. (83) and (86) of Sec. 2.

One of the main advantages of the use of spectral methods is the accuracy that we have in the interpolation inside the spectral domain. In the **ANETO** library this is done in the spectral representation, which involves transforming back and forth from the physical representation [see Eq. (67)]. The class **spectral_grid**<> computes the value of the function on any point of the spectral domain. For efficiency purposes, once they are computed, the spectral coefficients are stored inside the class so they can be used afterwards to get values of the function on another location without recomputing them. This can be done, not only for the values of a given function, but also for its first and second derivatives. In the library, this is used to incorporate a very efficient and accurate root finding algorithm inside the class. It is implemented with an iterative Newton's method to find the root until the precision of the datatype used is reached. If no root is present in the domain, the function will return the closest value, and if there is more than one, just one of them is returned.

B.2 Class Multidomain

The class **multidomain**<> generates a multidomain structure with the number of subdomains and collocation points per subdomain specified. The distribution of the subdomains can be chosen to be uniform or it can be fixed by specifying the location of their boundaries, which can be used to generate a mesh adapted to the resolution needs of the problem. The **multidomain**<> class manages the internal operations of the different subdomains and once it is created, its main features can be accessed without noticing the internal structure.

This class extends all the features present in the single domain class, increasing the functionalities in some aspects. For instance, the integration operations has the possibility of specifying the boundary condition on an arbitrary interior point, say x_C . Then, we can perform the integration according to the following expression

$$I_C(x) = I(x_C) + \int_{x_C}^x d\tilde{x} f(\tilde{x}). \quad (96)$$

The **multidomain**<> class also provides the opportunity of using the dual-grid scheme according to the Eq. (9) of Sec. 2.1. This option allows us to significantly improve the accuracy in the computation of derivatives at the points near the subdomain boundaries.

For the root finding operation, two important cases have been added. One for monotonically increasing functions and another one for monotonically decreasing functions. In both of them, the root, if it exists, will be unique. If there is no root in the whole computational domain, the function will return an error code. For general functions, we can find the root indicating the subdomain where we expect it to be located and the library returns the closest value even in the case that there is no root in the subdomain.

References

References

1. D. H. Bailey and J. M. Borwein, "High-Precision Arithmetic in Mathematical Physics," *Mathematics*, vol. 3, no. 2, p. 337, 2015.

2. G. Khanna, “High-Precision Numerical Simulations on a CUDA GPU: Kerr Black Hole Tails,” *J. Sci. Comput.*, vol. 56, pp. 366–380, Aug. 2013.
3. L. Lehner, “Numerical Relativity: A Review,” *Class. Quant. Grav.*, vol. 18, pp. R25–R86, 2001.
4. P. Grandclement and J. Novak, “Spectral methods for numerical relativity,” *Living Rev. Rel.*, vol. 12, p. 1, 2009.
5. M. Alcubierre, *Introduction to 3+1 Numerical Relativity*. International series of monographs on physics, Oxford: Oxford Univ. Press, 2008.
6. C. Bona, C. Palenzuela-Luque, and C. Bona-Casas, *Elements of Numerical Relativity and Relativistic Hydrodynamics: From Einstein’s equations to Astrophysical Simulations*. Berlin: Springer, 2009.
7. T. W. Baumgarte and S. L. Shapiro, *Numerical Relativity: Solving Einstein’s Equations on the Computer*. Cambridge: Cambridge University Press, 2010.
8. L. Lehner and F. Pretorius, “Numerical Relativity and Astrophysics,” *Ann. Rev. Astron. Astrophys.*, vol. 52, pp. 661–694, 2014.
9. V. Cardoso, L. Gualtieri, C. Herdeiro, and U. Sperhake, “Exploring New Physics Frontiers Through Numerical Relativity,” *Living Rev. Relativity*, vol. 18, p. 1, 2015.
10. C. Canuto, M. Y. Hussaini, A. Quarteroni, and T. A. Zang, *Spectral Methods: Evolution to Complex Geometries and Applications to Fluid Dynamics*. Springer Science & Business Media, 2007.
11. W. Bourke, *Spectral Methods in Global Climate and Weather Prediction Models*, pp. 169–220. Dordrecht: Springer Netherlands, 1988.
12. M. Ehrendorfer, *Spectral Numerical Weather Prediction Models*. Other titles in Applied Mathematics, Society for Industrial and Applied Mathematics, 2012.
13. D. Santos-Oliván and C. F. Sopena, “ANETO library: Arbitrary precision solver with pseudo-spectral methods.” <https://github.com/DSantos0/anetolib>, 2017.
14. D. Santos-Oliván and C. F. Sopena, “New Features of Gravitational Collapse in Anti-de Sitter Spacetimes,” *Phys. Rev. Lett.*, vol. 116, no. 4, p. 041101, 2016.
15. D. Santos-Oliván and C. F. Sopena, “Moving closer to the collapse of a massless scalar field in spherically symmetric anti-de Sitter spacetimes,” *Phys. Rev.*, vol. D93, no. 10, p. 104002, 2016.
16. C. Canuto, M. Y. Hussaini, A. Quarteroni, and T. A. Zang, *Spectral Methods in Fluid Dynamics*. Springer-Verlag, 1988.
17. J. P. Boyd, *Chebyshev and Fourier Spectral Methods*. New York: Dover, 2nd ed., 2001.
18. B. Fornberg, *A Practical Guide to Pseudospectral Methods*. Cambridge: Cambridge University Press, 1996.
19. R. Courant and D. Hilbert, *Methods of Mathematical Physics Volume II*. John Wiley and Sons, 1989.
20. F. John, *Partial Differential Equations*. New York: Springer Verlag, 1991.
21. W. H. Press, B. P. Flannery, S. A. Teukolsky, and W. T. Vetterling, *Numerical Recipes: The Art of Scientific Computing*. Cambridge (UK) and New York: Cambridge University Press, 1992.
22. C. Canuto, M. Y. Hussaini, A. M. Quarteroni, and Z. T. Jr, *Spectral Methods. Fundamentals in Single Domains*. Berlin Heidelberg: Springer-Verlag, 2006.
23. L. Dagum and R. Menon, “OpenMP: an industry standard API for shared-memory programming,” *Computational Science & Engineering, IEEE*, vol. 5, no. 1, pp. 46–55, 1998.
24. M. Joldes, J.-M. Muller, V. Popescu, and W. Tucker, “CAMPARY: Cuda Multiple Precision Arithmetic Library and Applications,” in *5th International Congress on Mathematical Software (ICMS)*, (Berlin, Germany), July 2016.
25. C. Runge, “Über empirische Funktionen und die Interpolation zwischen äquidistanten Ordinaten,” *Zeitschrift für Mathematik und Physik*, vol. 46, pp. 224–243, 1901.
26. J. Epperson, “On the Runge example,” *Amer. Math. Monthly*, vol. 94, pp. 329–341, 1987.
27. S. W. Hawking and G. F. R. Ellis, *The Large Scale Structure of Space-Time*. Cambridge: Cambridge University Press, 1973.
28. C. W. Misner, K. Thorne, and J. A. Wheeler, *Gravitation*. San Francisco: W. H. Freeman & Co., 1973.
29. R. M. Wald, *General Relativity*. Chicago: The University of Chicago Press, 1984.
30. E. Poisson, *A Relativist’s Toolkit. The Mathematics of Black-Hole Mechanics*. Cambridge: Cambridge University Press, 2004.
31. B. F. Schutz, *Geometrical Methods of Mathematical Physics*. Cambridge: Cambridge University Press, 1980.

32. A. Einstein, “Feldgleichungen der Gravitation,” *Sitzungsberichte der Preussischen Akademie der Wissenschaften zu Berlin*, vol. Part 2, pp. 844–847, 1915.
33. H. Stephani, D. Kramer, M. MacCallum, C. Hoenselaers, and E. Herlt, *Exact solutions of Einstein’s field equations*. Cambridge: Cambridge University Press, 2003.
34. H. S. Reall, N. Tanahashi, and B. Way, “Shock Formation in Lovelock Theories,” *Phys. Rev.*, vol. D91, no. 4, p. 044013, 2015.
35. E.ourgoulhon, “3+1 Formalism and Bases of Numerical Relativity,” 2007.
36. M. W. Choptuik, “Universality and scaling in gravitational collapse of a massless scalar field,” *Phys. Rev. Lett.*, vol. 70, pp. 9–12, 1993.
37. B. Szilagyi, L. Lindblom, and M. A. Scheel, “Simulations of Binary Black Hole Mergers Using Spectral Methods,” *Phys. Rev.*, vol. D80, p. 124010, 2009.
38. R. Haas *et al.*, “Simulations of inspiraling and merging double neutron stars using the Spectral Einstein Code,” *Phys. Rev.*, vol. D93, no. 12, p. 124062, 2016.
39. P. Canizares and C. F. Sopena, “An Efficient Pseudospectral Method for the Computation of the Self-force on a Charged Particle: Circular Geodesics around a Schwarzschild Black Hole,” *Phys. Rev.*, vol. D79, p. 084020, 2009.
40. P. Canizares, C. F. Sopena, and J. L. Jaramillo, “Pseudospectral Collocation Methods for the Computation of the Self-Force on a Charged Particle: Generic Orbits around a Schwarzschild Black Hole,” *Phys. Rev.*, vol. D82, p. 044023, 2010.
41. R. Panosso and M. Ansorg, “Axisymmetric fully spectral code for hyperbolic equations,” *J. Comput. Phys.*, vol. 276, pp. 357–379, 2014.
42. M. Oltean, C. F. Sopena, and A. D. A. M. Spallicci, “Particle-without-Particle: a practical pseudospectral collocation method for linear partial differential equations with distributional sources,” *Journal of Scientific Computing*, Nov 2018.
43. C. Gundlach, “Critical phenomena in gravitational collapse,” *Phys. Rept.*, vol. 376, pp. 339–405, 2003.
44. C. Gundlach and J. M. Martin-Garcia, “Critical phenomena in gravitational collapse,” *Living Rev. Rel.*, vol. 10, p. 5, 2007.
45. D. Christodoulou, “The Problem of a Self-gravitating Scalar Field,” *Commun. Math. Phys.*, vol. 105, pp. 337–361, 1986.
46. D. S. Goldwirth and T. Piran, “Gravitational Collapse of Massless Scalar Field and Cosmic Censorship,” *Phys. Rev.*, vol. D36, p. 3575, 1987.
47. D. Garfinkle, “Choptuik scaling in null coordinates,” *Phys. Rev.*, vol. D51, pp. 5558–5561, 1995.
48. P. Bizoń and A. Rostworowski, “On weakly turbulent instability of Anti-de Sitter space,” *Phys. Rev. Lett.*, vol. 107, p. 031102, 2011.
49. M. Choptuik, J. E. Santos, and B. Way, “Charting Islands of Stability with Multioscillators in anti-de Sitter space,” *Phys. Rev. Lett.*, vol. 121, no. 2, p. 021103, 2018.
50. J. H. Verner, “Explicit runge-kutta methods with estimates of the local truncation error,” *SIAM Journal on Numerical Analysis*, vol. 15, no. 4, pp. 772–790, 1978.
51. P. J. Prince and J. R. Dormand, “High order embedded Runge-Kutta formulae,” *Journal of Computational and Applied Mathematics*, vol. 7, no. 1, pp. 67–75, 1981.
52. J. Hennig and M. Ansorg, “A Fully Pseudospectral Scheme for Solving Singular Hyperbolic Equations on Conformally Compactified Space-Times,” *J. Hyperbol. Diff. Equat.*, vol. 6, p. 161, 2009.
53. J. Hennig, “Fully pseudospectral time evolution and its application to 1+1 dimensional physical problems,” *J. Comput. Phys.*, vol. 235, pp. 322–333, 2013.
54. B. Gustafsson, H.-O. Kreiss, and J. Olinger, *Time Dependent Problems*. New York: John Wiley & Sons, 1995.
55. A. Bayliss and E. Turkel, “Mappings and accuracy for Chebyshev pseudo-spectral approximations,” *Journal of Computational Physics*, vol. 101, no. 2, pp. 349 – 359, 1992.
56. D. Kosloff and H. Tal-Ezer, “Modified Chebyshev Pseudospectral method with $O(N^{-1})$ Time Step Restriction,” *J. Comput. Phys.*, vol. 104, pp. 457–469, 1993.
57. R. Peyret, *Spectral methods for incompressible viscous flow*, vol. 148. Springer Science & Business Media, 2013.
58. J. Maddock and C. Kormanyos, “Boost Multiprecision Library.” http://www.boost.org/doc/libs/1_66_0/libs/multiprecision/doc/html/index.html, 2002.
59. L. Fousse, G. Hanrot, V. Lefèvre, P. Pélissier, and P. Zimmermann, “MPFR: A Multiple-precision Binary Floating-point Library with Correct Rounding,” *ACM Trans. Math. Softw.*, vol. 33, June 2007.
60. P. Holoborodko, “MPFR C++.” <http://www.holoborodko.com/pavel/mpfr/>, 2008-2012.
61. G. Guennebaud, B. Jacob, *et al.*, “Eigen v3.” <http://eigen.tuxfamily.org>, 2010.